

MeqSilhouette : A mm-VLBI observation and signal corruption simulator

Dissertation presented in fulfillment of the requirements for the
degree of
MASTER OF SCIENCE
in the Department of Physics and Electronics
Rhodes University

Author:

Tariq BLECHER

Department of Physics and

Electronics, Rhodes University

Supervisors:

Roger DEANE

Gianni BERNARDI

Oleg SMIRNOV

*Department of Physics and
Electronics, Rhodes University*

July 28, 2016

Abstract

Acknowledgements

Plagiarism

I acknowledge that plagiarism is wrong and hereby declare that the work contained in this document and in the supporting software is my own, save for that which is properly acknowledged.

Tariq Dylan Blecher

The source code for the imaging software package (along with its full development history) accompanying this document is publicly available on the Rhodes University Radio Astronomy Techniques and Technologies software repository at . As such no part of the source code will be printed in this document.

Contents

| | |
|---|------------|
| Abstract | iii |
| Acknowledgements | iv |
| Plagiarism | v |
| 1 Introduction | 2 |
| 1.0.1 Science with increasing resolution | 2 |
| 1.0.2 Very Long Baseline Interferometry | 2 |
| 1.0.3 The Event Horizon Telescope (EHT) | 4 |
| 1.0.4 Scientific opportunities with the EHT | 4 |
| 1.0.5 Challenges and obstacles in mm-VLBI observations | 6 |
| 1.0.6 Science extraction : parameter estimation and imaging | 6 |
| 1.0.7 A realistic mm-VLBI simulator | 6 |
| 2 Theoretical background | 9 |
| 2.0.8 Radio Interferometry | 9 |
| 2.1 Signal Corruptions | 11 |
| 2.1.1 Scattering basics | 11 |
| 2.2 Interstellar medium scattering | 13 |
| 2.3 Troposphere | 17 |
| 2.3.1 Propagation through a linear medium | 17 |
| 2.3.2 Average atmosphere | 18 |
| 2.3.3 Turbulent atmosphere | 20 |
| 2.3.4 Instrumental | 21 |
| 3 Software architecture and implementation | 24 |
| 3.1 Simulator | 24 |
| 3.1.1 ScatterBrane | 25 |
| 3.1.2 Atmospheric | 26 |
| 3.1.3 Pointing | 27 |
| 3.1.4 RODRIGUES interface | 28 |
| 3.2 Parameter estimation | 28 |
| 4 Results and analysis | 29 |
| 4.0.1 Canonical simulations | 29 |
| 4.0.2 Parameter estimation | 34 |
| 5 Conclusion | 35 |

List of Figures

| | | |
|-----|---|----|
| 1.1 | The young stellar system HL Tau, observed at 223 GHz by ALMA. The orbits of forming planets appear as dark rings cut out of the disk. The presence of these bodies are surprising given that host star is still very young. The detail in this image was made possible by the milliarcsec resolution achievable with ALMA. | 3 |
| 1.2 | (Image credit: Remo Tilanious) Event Horizon Telescope uses Earth-diameter baselines to attain resolution $\sim 10 \mu\text{arcsec}$ | 4 |
| 2.1 | Illustration depicting the basics of scattering in the weak (left) and strong (right) regimes. In the weak regime, the signal is coherently propagated over an area, $A_{\text{weak}} \approx \pi r_F^2$ whereas in the strong regime, coherent propagation is split over many areas of size $A_{\text{strong}} \approx \pi r_0^2$ | 12 |
| 2.2 | The λ^2 dependence of scattering kernel size is shown by the solid line. This has been derived from measurements made at $\lambda > 17 \text{ cm}$ [5]. The dotted line shows the derived intrinsic source size which scales as $\lambda^{1.44}$. This was derived from measurements in the wavelength range, $2 \text{ cm} < \lambda < 1.3 \text{ mm}$. The red circles show major-axis observed sizes of Sgr A* and the green points show the derived intrinsic major-axis size. This plot was reproduced from (author?) [15]. | 14 |
| 2.3 | Closure phases recorded in a VLBA + LMT observation of Sgr A* at $\lambda = 3.5 \text{ mm}$ [?]. The data points are shown as red circles and blue squares and are only distinguished by the calibrator used. The green envelopes show the 1σ closure phase prediction induced by scattering-induced substructure. Reproduced from ?] | 17 |
| 2.4 | A cartoon illustration of poorly mixed water vapour moving over a baseline (credit : Thompson et al, ibid) | 21 |
| 2.5 | showing β changes with distance on the phase screen. Note the three distinct regime but continuous variation in between | 22 |

- 3.1 Flow diagram showing basic sequence of the MEQSILHOUETTE simulation pipeline. The sky model could include (a) a time-ordered list of FITS images or (b) parametric source model consisting of Gaussians or point sources. The details of the station information, observation strategy, tropospheric and ISM conditions are specified in a user-defined input configuration file. The pipeline is flexible, allowing any additional, arbitrary Jones matrices to be incorporated. Further details in text. 25
- 4.1 An example simulation of ISM scattering towards Sgr A*. The top panel, left to right, shows the original FWHM = 40 μ -arcsec Gaussian (**top left**), the ISM scattered image on the first night (**top middle**) and last night (**top right**) of the observation respectively. The bottom panel, left to right, shows the evolution of the 10 minute-averaged closure phase with epoch (**bottom left**), *uv*-tracks for any particular night (**bottom middle**) and the visibility amplitudes $|V|$ of the unscattered (red) and scattered (grey-scale) sources as a function of *uv*-distance (**bottom right**). Variations of the flux on the shortest baselines reveal total flux modulation while flux variations $\Delta|V|$ on longer baselines and non-zero closure phases track the fluctuations in refractive noise. When compared to the latest published observations of Sgr A* [17], we see that the observed and simulated closure phase variability are consistent. Furthermore, ISM scattering simulations can constrain the variability fraction associated with the screen, enabling a more robust estimation of source variability. . . 30
- 4.2 Best fit opacity (red) and sky brightness temperature (blue) line solutions at $\nu = 230$ GHz as a function of precipitable water vapour (PWV) for three indicative ground pressures and temperatures which approximately represent the sites of SPT (solid), ALMA (diamond) and SMA (dashed). The legend shows the estimated input ground (pressure, temperature) parameters for each site. 31
- 4.3 Simulation of the total delay (left) and the turbulent atmospheric delay (right) for SMA (blue) and ALMA (green) sites towards Sgr A*. Ground pressures and temperatures are the same as Fig. 4.2, precipitable water vapour above each station is set to $w = 2$ mm, and the instantaneous zenith coherence time is set $T_0 = 10$ s for both stations. Note that all tropospheric parameters are, however, independently set. The conversion from time delay to phase at 230 GHz is 1 rad = 0.7 ps. 31

- 4.4 The effect of residual troposphere phase noise on interferometric images of a point source observed for 12 hours at 230 GHz with 4 GHz bandwidth with the following array : SPT, ALMA, SMA, SMT, LMT and JCMT, assuming the same SEFDs as (**author?**) [28] and an elevation limit of 15° . For simplicity the weather parameters at each station were set to: coherence time $t_0 = 10$ sec; PWV depth $w = 1$ mm; ground pressure $P = 600$ mb; ground temperature $T = 273$ K. **Top left:** interferometric map with thermal noise only. **Top right:** atmospheric attenuation and sky noise (due to non-zero opacity) with 1% of the turbulent phase noise added. **Bottom left:** as previous but with 3% of turbulent phase contribution. **Bottom right:** as previous but with 6% turbulent phase contribution. The fractional turbulent phase contributions are illustrative of the effect of fringe-fitting errors. Note the decrease in the source peak flux with increasing turbulent tropospheric phase noise. Note further that the peak source centroid is offset from its true position (black crosshairs).
- 4.5 RMS relative amplitude error induced by pointing error with the 50 m (i.e. fully illuminated) LMT antenna as a function of pointing error offset ρ at 230 GHz. We assume that these errors are degenerate or non-separable from the self-calibration/fringe-fitting model used. See text for the description of the three models used. This simulation capability enables constraints on the magnitude of pointing-induced errors given a particular pointing calibration strategy.

32

33

List of Tables

- 2.1 A re-analysis of VLBI observations of Sgr A* by ?] has yielded revised estimates of the parameters associated with the Gaussian scattering kernel. An accurate estimation is needed for accurate extrapolation to 1.3 mm. Note that the position angle is measured East of North.

13

Chapter 1

Introduction

1.0.1 Science with increasing resolution

Throughout the history of astronomy, we see celestial sources which appear point-like or unresolved with the instrumentation available at the time. To study these sources in enough detail to clarify their nature, ever more sophisticated instruments have to be developed.

These instruments span the electromagnetic spectrum, and here I recall several notable examples which illustrate the discovery potential of an increase in resolution.

At optical wavelengths, the Hubble Space Telescope was able to resolve the gravitational sphere of influence of the central supermassive black hole (SMBH) in nearby galaxies. These measurements uncovered the fundamental relations between black hole mass and both stellar bulge luminosities and velocity dispersions (Ferrasse and Merritt (2000), Gebhardt et al. (2000)) which has been a foundation for extra-galactic astronomy ever since.

A more recent example is a 2014 science verification result with the Atacama Large Millimetre Array (ALMA) [8] which resolves the molecular dust disk surrounding the young protostellar system, HL Tau Fig. 1.1. This observation showed, in unique detail, the orbit cleared out by forming planets which was surprising given that the stellar system was so young. The clarity of the image surpasses all previous work on the subject and provides a strong science case for conducting observations of similar systems with ALMA.

X-ray wavelengths with Chandra, we see the bullet cluster (Clowe 2004,)

The technique which achieves the highest resolution is Very Long Baseline Interferometry (VLBI)

1.0.2 Very Long Baseline Interferometry

VLBI is network

The development of VLBI, originated in the late 1960's with observations of compact, highly-variable objects, now known as quasars. Teams using VLBI discovered that these objects consist of core-jet systems. Also the presence of super-luminal jet motion. *TMS copy, paste : By using local oscillators at each antenna that are controlled by high-precision frequency standards, it is possible to preserve the coherence of the signals for time intervals long enough to measure interference fringes. The received signals are converted to an intermediate*

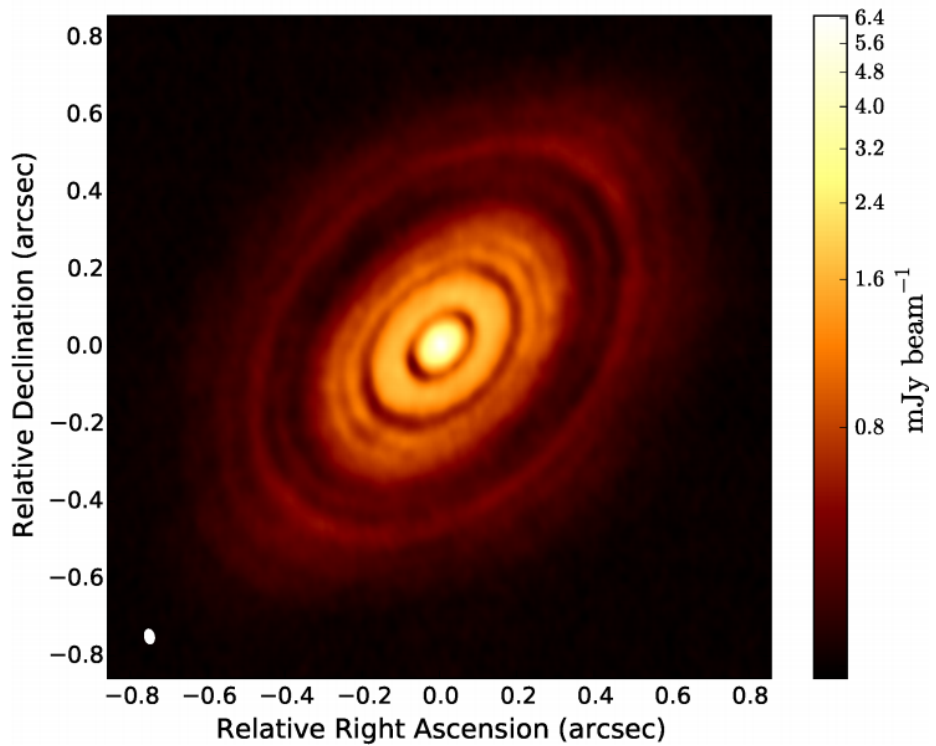


Figure 1.1: The young stellar system HL Tau, observed at 223 GHz by ALMA. The orbits of forming planets appear as dark rings cut out of the disk. The presence of these bodies are surprising given that host star is still very young. The detail in this image was made possible by the milliarcsec resolution achievable with ALMA.

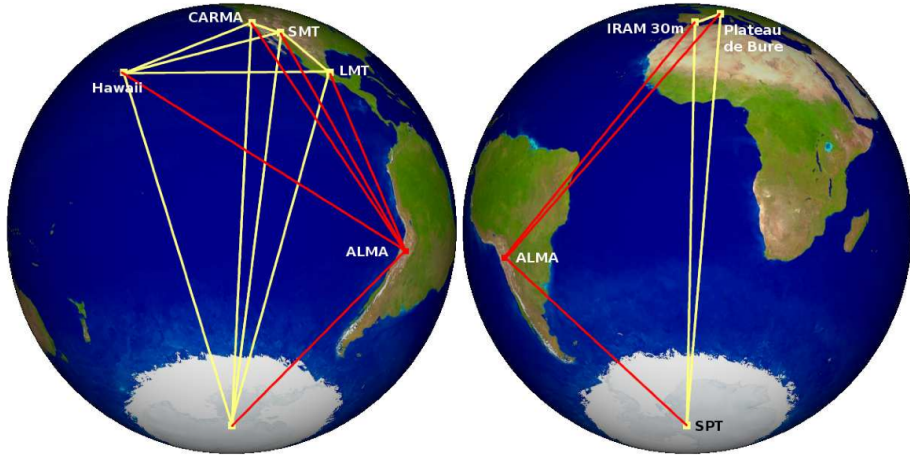


Figure 1.2: (Image credit: Remo Tilanius) Event Horizon Telescope uses **Earth-diameter baselines** to attain **resolution** $\sim 10 \mu\text{arcsec}$.

frequency low enough that they can be recorded directly on magnetic tape, and the tapes are subsequently brought together and played into a correlator.

Examples of Arrays : Very Long Baseline Array (VLBA) : 1.4 - 87 GHz, European VLBI Network (EVN), African VLBI Network (AVN).

1.0.3 The Event Horizon Telescope (EHT)

This thesis is centred around such a class of emerging early 21st century instrumentation, known as Very Long Baseline Interferometry at millimetre wavelengths (mm-VLBI). This technique enables angular resolution on the order of $\sim 10 \mu\text{-arcsec}$ by maximising both antenna separation and observing frequency. The sub-field is being led by the Event Horizon Telescope consortium (EHT), an international project whose primary objective is to resolve the supermassive black holes (SMBH) located at the centre on our Galaxy, known as Sagittarius A* (Sgr A*), and M87 on angular scales comparable to the black hole event horizon. This thesis aims to contribute to the EHT objectives through algorithmic development of data simulation and parameter estimation pipelines, which are particularly relevant given the significant calibration challenges faced by the project.

1.0.4 Scientific opportunities with the EHT

To constrain the physics near a black hole, the observation needs to be sensitive to scales comparable to the event horizon. For the case of a non-spinning or Schwarzschild black hole, the event horizon is spherically symmetric with a radius, $R_{\text{Sch}} = 2GM_{\text{BH}}/c^2$, where M_{BH} is the black hole mass, G is the gravitational constant and c is the speed of light. The angular size of such an event horizon in the far field approximation is $\theta_{\text{Sch}} = R_{\text{Sch}}/D \approx 0.02 \text{ nanoarcsec} (M_{\text{BH}}/M_{\odot})(\text{kpc}/D)$ where D is the distance from observer to source. For SMBH's Sgr A* and M87, this results in $\theta_{\text{Sch}} \sim 5 - 10 \mu\text{-arcsec}$. The event

horizon telescope will have baseline lengths $|b| \sim 10^3$ km and is currently observing at $\nu = 230$ GHz, yielding a diffraction-limited angular resolution of $\theta_{\text{EHT}} = 1.22\nu/|b| \approx$. Hence EHT will be able to resolve these objects on the scale of the event horizon/gravitational radius.

Equally important to that the millimetre emission is optically thin and therefore probes inner emission region. The power spectrum of Sgr A* peaks in sub-mm bump. Synchtron emission. Lensed emission. the interferometric technique also filters out smooth mm emission.[Read Falke 1998]

FIG. basic grmhd image of black hole shadow, scale indicating resolution and eht beam size

Strong gravity and black hole spacetime

Gravity as described by General Relativity (GR) has flawlessly agreed with all observational experiments, however GR has conceptual weaknesses, especially as it is not compatible with the quantum description of reality. Various alternatives to GR have been theorised which do not assume a purely classical description of matter. To test GR against its numerous alternatives, we have to observe gravity in the regime where we expect the largest observational deviations a GR prediction would have if it were only an approximate theory of gravity. The spacetime close to a SMBH is an ideal candidate, as the gravitational effects are very strong. Lensed emission of the gravitational lensed photon ring. The exact sizes and shapes of which indicate different spacetime and theories of gravity. Note that even in this regime, the deviation from GR is small. We can also explore black hole physics by testing the no-hair theorem or that black holes are only described by their mass, spin and charge by constraining the quadrupole moment of the black hole.deviations from the Kerr metric

FIG. Plot of analytic shapes and sizes of the bh shadow from the predictions of different theories of gravity

AGN accretion and jet launch astrophysics

[AGN jet basics.]

Astrophysical jets were first discovered over a century ago, accretion onto a black hole was first postulated to power these jet by .. .However a century later, the mechanism of accretion and jet launching ifrom SMBH are still highly debated.

Fig: Typical AGN jet illustration showing magnetic fields

Recently an industry of sophisticated General Relativistic Magneto-Hydrodynamic (GRMHD) simulations has developed yielding important insights but also new questions. Now, mm-VLBI has the opportunity of constrains the mechanisms. Specifically we can map the magnetic field configuration, which is a key aspect using polarimetry and Faraday Rotation. The quiescent and variability structure and also be explore in total intensity. Flaring structure. Distinguish between accretion disk and inner jet. Distinguish between the different Jet and Disk models for each bh. Deterimine spin.

Fig: 2/3 panels of simulated images of disk and jet models of Sgr A*/M87

In M87, where the jet is dominant, micro-arcsecond scale astrometry, capable with the EHT, can determine the distance from the jet base from the event horizon, as well as the width of the jet base. Opening up new possibilities in explore particle production and other exotic physics occurring at the event horizon.

Fig: 2/3 panels of simulated polarimetric images of Sgr A*/M87 showing ordered magnetic fields

1.0.5 Challenges and obstacles in mm-VLBI observations

Performing Very Long Baseline Interferometry (VLBI) at mm-wavelengths presents unique calibration challenges, including very short atmospheric coherence times that are typically $\lesssim 10$ s [14], low calibrator source sky density, complex and variable calibrator source structure, and antenna pointing accuracies that are a non-negligible fraction of the antenna primary beam. Addition These effects may place significant limitations on the sensitivity, image fidelity, and dynamic range that can be achieved with mm-VLBI. Performing mm-VLBI however, is a difficult task for a variety of reasons. Firstly the arrays are inhomogenous, made up of a collections of different stations working together, Difficult to get time on all the stations. there are a variety of signal corruptions which take place. Briefly introduce signal corruptions, variability, ..etc, how these represent calibration and interpretation challenges.

1.0.6 Science extraction : parameter estimation and imaging

we need to measure the fractional asymmetry of the shadow shape with respect to its angular size to the few percent

Estimating the ‘macro’-parameters of Sgr A*, spin, orientation, position angle through a Bayesian parameter estimation analysis with closure quantities Furthermore, unaccounted for systematic and/or non-Gaussian uncertainties could preclude robust, accurate Bayesian parameter estimation and model selection analyses of accretion flow [e.g. 6] and gravitational physics [e.g. 7, 38], two of the EHT’s many objectives.

see psaltis 2015 for some other shadow detection criteria **Fig: A Broderick 2016 posterior probability distribution (?)**

1.0.7 A realistic mm-VLBI simulator

Given the significant observation challenges that the EHT faces, we have undertaken this project to build a mm-VLBI observation and signal corruption simulator. There are many benefits for using such a toolkit and indeed synthetic data simulation is common practice for every major scientific experiment. Two prominent examples is the extensive synthetic data generation for gravitational wave template matching for LIGO (ref) or for LHC particle collision experiments (ref). In essence such a simulator would fill in the final part of

the theoretical signal propagation chain, effectively taking astrophysical simulations of the source (e.g. SMBH) as an input and returning realistic synthetic data. This allows a more effective interplay between theory and observation. The remainder of this section will briefly discuss several use cases for an EHT synthetic data simulator and how we have designed the software to meet these requirements.

A key observational use case is the testing of calibration, parameter estimation and imaging algorithms and strategies. As the inputs to the simulator are known exactly, when passing simulated data through the data processing pipelines, we are better able to explore sources of error which are difficult to disentangle from intrinsic source features in real data. A straightforward way to perform such a test is through the creation of a set of ‘standard challenge’ dataset. Such datasets would be available to the entire community input into their calibration and/or imaging routines. Following this, a detailed comparison between the different strategies in varying regimes (source and other factors) can be made. Importantly, a systematic investigation of a particular algorithm across many different datasets could provide insight into subtle or previously unknown sources of error.

Bayesian parameter estimation and model selection analyses of accretion flow [e.g. 6] and gravitational physics [e.g. 7, 38] offer a promising approach to constrain theoretical models when using visibilities or visibility derived quantities. However, unaccounted systematic errors in the signal processing chain could bias the posterior probability distribution, precluding a robust and accurate determination of key science parameters. Through the construction of an end-to-end simulation pipeline, the Bayesian parameter estimation procedure extended to handle more realistic synthetic data. This would entail combining many iterations data simulator with a solver to perform calibration and parameter estimation.

Simulated data can also assist in the optimisation of the experimental configuration. Financial constrains require the prioritisation of hardware upgrades e.g. increasing bandwidth, surface accuracy improvement, deployment of water vapour radiometers or additional receiver bands. Simulated data together with calibration and imaging pipelines can help to quantify the benefit of each improvement based on expected scientific return. This approach can even be extended to assess new candidate stations, especially as new geographic locations e.g. in Southern Africa are receiving increasing attention due to the potential long baselines to ALMA, SPT and European stations.

Recently, there has been an increase in the attention given to simulating EHT observations of Sgr A* ((**author?**) 18; (**author?**) 28; (**author?**) 3). However, these are primarily focused on image reconstruction and assume perfect phase calibration i.e. no troposphere-induced fringe-fitting errors; perfect antenna pointing accuracy; perfect phasing efficiency; and in most cases simple, non-variable Gaussian kernel smoothing to simulate ISM scattering. Clearly, as the EHT array is enhanced (and likely expanded), so too must the interferometric simulations evolve to provide ever-more realistic predictions on the confidence levels with which parameters can be extracted and hence exclude theoretical models of gravity and/or accretion flows.

Over the past decade, significant effort has been placed on advanced radio interferometric calibration and imaging algorithms for centimetre and metre-wave facilities in response to the large number of new arrays in construction

or design phase (e.g. MeerKAT, ASKAP, SKA, LOFAR, HERA). A leading software package in this pursuit is MEQTREES¹ [34], which was developed to simulate, understand and address the calibration issues to be faced with the greatly enhanced sensitivity, instantaneous bandwidth, and field-of-view of such facilities. For example, MEQTREES is rooted in the Measurement Equation mathematical formalism [21], which parameterizes the signal path into distinct 2×2 complex matrices called Jones matrices. This formalism and applications thereof are laid out in [42, 43, 44] and are arbitrarily generalized to model any (linear) effect, including undesired signal corruptions that often may have subtle yet systematic effects. MEQTREES has been applied to correct for direction dependent calibration errors to JVLA and WSRT observations, achieving record-breaking high dynamic range images [44]. The effectiveness provided by the Measurement Equation formalism in radio interferometric calibration provides a strong motivation to explore its application to challenging goal of imaging a supermassive black hole silhouette with mm-VLBI. To construct this simulator we leverage off metre and cm-wavelength simulation and calibration successes and build a MEQTREES-based mm-VLBI-specific software package which we name, MEQSILHOUETTE. Use of MEQTREES and MEASUREMENT SET data format lends itself to investigating a range of different techniques that are used in other areas of interferometry (e.g. coh-Jones paper). While MEQTREES has not yet been used in the context of mm-wavelength observations, the framework is agnostic to higher frequency implementation as long as the Measurement Equation is appropriately constructed. This technology enables us to understand a wide range of mm-VLBI signal propagation and calibration systematics, quantify their effect on accretion flow and gravitational theoretical model selection, and hence maximise the scientific utility from EHT observations.

¹<https://ska-sa.github.io/meqtrees/>

Chapter 2

Theoretical background

Our goal, is to add the final steps in the theory chain which transforms the GRMHD simulations into interferometric observables. For this to be achieved and for the theory higher up in the chain to be maximally useful in data interpretation, realistic signal corruptions need to be considered. Hence, the purpose of this module is to further the sophistication of the interplay between theory and observation in the field. The signal corruptions which we have identified as the most prominent occurs in the troposphere, interstellar medium (ISM) and within the stations themselves. First I will review some EM wave fundamental and introduce scattering theory, which is applicable to both the radiative process occurring in the troposphere and ISM. Following the general introduction I will explore each specific case.

2.0.8 Radio Interferometry

Measurement Equation

mm-VLBI observables and data products

If the visibility phase is highly variable as in the case of a turbulent atmosphere, conventional calibration and imaging techniques have severely limited (if any) success. However information can still be extracted from the raw visibilities in the form of closure quantities [30] or polarisation ratios [?]. Closure phase, defined as the sum of 3 visibility phases of a triangle of stations $\{i, j, k\}$, is a probe of asymmetry in source structure,

$$\Phi_{ijk} = \phi_{ij} + \phi_{jk} + \phi_{ki}. \quad (2.1)$$

Because most signal corruptions are station based, the gain phase terms $\phi_{ij} = \phi^{\text{true}} + \phi_i^G - \phi_j^G$ for each antenna will cancel, yielding a more robust observable.

The uncertainty on the closure phase is model dependent [40] and is given as a function of the SNR s of each baseline

$$u(\Phi_{ijk}) = \frac{\sqrt{4 + (s_{ij}s_{jk})^2 + (s_{jk}s_{ki})^2 + (s_{ij}s_{ki})^2 + 2(s_{ij}^2 + s_{jk}^2 + s_{ki}^2)}}{s_{ij}s_{jk}s_{ki}}, \quad (2.2)$$

where s_{ij} is defined as

$$s_{ij} = |V_{ij}| \sqrt{\frac{\tau \Delta\nu}{SEFD_i SEFD_j}}, \quad (2.3)$$

where τ is the vector averaging timescale, $\Delta\nu$ is the bandwidth, $|V_{ij}|$ is the visibility amplitude and $SEFD$ is the system equivalent flux density. The result that closure phase is entirely immune to station based effects breaks down however when time averaging in the presence of baseline dependent effects like thermal noise as illustrated in section ??.

Variability and the static source assumption

Implicit in our description of interferometry above, we assumed that the source remains approximately unchanged or static during the course of the observation. However, if this assumption does not hold (i.e. if the source is time-variable), the visibilities measured over the course of an observation can no longer be related to a single image and if they are, the resulting image would appear smeared out as it is averaged over many realisations. Note that I am using the term ‘variability’ in a general sense which refers to changes in any source observables. Most commonly variability is refers to changes in source flux (visibility amplitude) but I include changes in source structure and position (visibility phase) and source polarisation. Practically it is difficult to separate source and instrumental variability without accurate models and measurements for all non-source signal propagation effects. Although the static source assumption holds for most interferometric observations, the accretion flow and/or magnetic field structures around a SMBH can be variable on far shorter timescales. The primary mm-VLBI target, Sgr *, exhibits variability on timescales of minutes to hours in the radio (including in EHT observations), near-infrared (NIR), and X-ray bands [e.g. ? ? ? ? 16, 23]. This wealth of observational data has yielded several answers but the origin of the variability is still highly debated. To explain the observed delays between flares in different frequency bands, an expanding adiabatic plasma model (Marrone, 2008) has been presented however a recent flare observed with the EHT did not exhibit the increase in size expected from an expanding plasma outflow model [16]. Signatures of periodic variability at NIR and x-ray [?] have been used to argue for the presence of orbiting hotspots [14]. As the Innermost Stable Circular Orbit (ISCO) depends on spin of the BH, the spin can be constrain through the detection periodic orbital features. However a longer light curve in the NIR is more representative of a power-law scale variability [?]. These observations point to the possibility of multiple flaring mechanisms. An important mm-VLBI observational result is that variability in the polarisation domain is far more rapid than the total intensity (Johnson 2015b), indicating the presence of highly variable magnetic fields. In principle, the variability timescale can be comparable to the period of the Innermost Stable Circular Orbit (ISCO), which for Sgr A*, ranges from 4 minutes in the maximally rotating realisation to about half an hour for a non-rotating BH. The ISCO period for M87 is longer on the order of day scales. Considering light crossing times Δt_{cross} , we can estimate the angular size θ of the emission region to be of order $\theta \sim \Delta t_{\text{cross}} c / D_{\text{src}}$, where c is the speed of light and D_{src} is the observer-source distance. Hence for Sgr * at a distance of 8.3 kpc

(Gillessen, 2009), for a flare of duration $\Delta t_{\text{cross}} = 10$ min, which corresponds to scales of $15R_{\text{Sch}}$, further evidence of emission areas close the event horizon. If a flare is dominated by a localised variable structure, several approaches [14? ?] show that EHT can track flaring structures with $\sim 5 \mu\text{-arcsec}$ precision using closure quantities and polarimetric ratios which could help map the spacetime around the BH. Alternatively ?] show that a gaussian weighting scheme can be applied to mitigate the effects of variability and measure the quiescent structure although approach would downweight the longest baselines. However all of these approaches assume only gaussian thermal noise, gaussian-blurring in the ISM and no fringe-fitting errors.

2.1 Signal Corruptions

2.1.1 Scattering basics

Millimetre wavelength radiation originating at the Galactic Centre is repeatedly scattered along the signal path to the Earth-based observer. The first occurrence is due to electron plasma in the interstellar medium (ISM) ((author?) 5, (author?) 20), while the second is due to poorly-mixed water vapour in the Earth's troposphere ((author?) 9, (author?) 27). It is essential that the effects of the scattering phenomena are understood for a rigorous calibration and interpretation of data. Towards this end, simulation modules approximating scattering in both media are implemented in MEQSILHOUETTE. As an introduction to the separate descriptions of each, we review a simple scattering model.

An electro-magnetic wave is scattered when it passes through a medium with refractive index inhomogeneities. Following (author?) [31], this effect can be modeled as a thin screen, located between source and observer planes and orientated perpendicular to the line-of-sight. The screen, indexed by coordinate vector \mathbf{x} , adds a stochastic phase $\phi(\mathbf{x})$ to the incoming wave at each point on the screen, yielding a corrugated, outgoing wavefront. We define the Fresnel scale as $r_F = \sqrt{\lambda D_{\text{os}}/2\pi}$, where D_{os} is the observer-scatterer distance, or the distance where the geometrical path difference $\frac{2\pi}{\lambda}(D_{\text{os}} - \sqrt{D_{\text{os}}^2 + r_F^2}) = \frac{1}{2} \text{ rad}$.

To determine the resultant electric field at a point in the plane of the observer, indexed by coordinate vector \mathbf{X} , one has to take into account all possible ray paths from the screen to \mathbf{X} . To illustrate the model, a calculation of the scalar electric field generated by a point source, $\psi(\mathbf{X})$ yields the Fresnel-Kirchoff integral [2]

$$\psi(\mathbf{X}) = C \int_{\text{screen}} \exp \left[i\phi(\mathbf{x}) + i\frac{(\mathbf{x} - \mathbf{X})^2}{2r_F} \right] d\mathbf{x}, \quad (2.4)$$

where C is a numerical constant.

The statistics of $\phi(\mathbf{x})$ can be described by a power spectrum or equivalently the phase structure function,

$$D_\phi(\mathbf{x}, \mathbf{x}') = < [\phi(\mathbf{x} + \mathbf{x}') - \phi(\mathbf{x})]^2 >, \quad (2.5)$$

where \mathbf{x} and \mathbf{x}' represent two points on the screen and $<>$ denotes the ensemble average.

There is evidence that D_ϕ can be reasonably approximated by a power law dependence on the absolute distance r between points on the screen [1, 10]

$$D_\phi(r) = (r/r_0)^\beta, \quad r^2 = \mathbf{x}^2 - \mathbf{x}'^2 \quad (2.6)$$

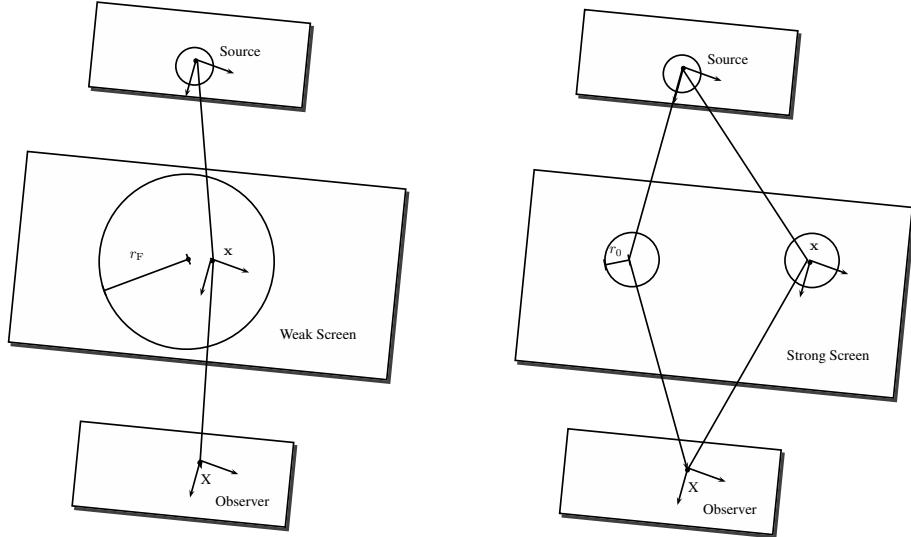


Figure 2.1: Illustration depicting the basics of scattering in the weak (left) and strong (right) regimes. In the weak regime, the signal is coherently propagated over an area, $A_{\text{weak}} \approx \pi r_F^2$ whereas in the strong regime, coherent propagation is split over many areas of size $A_{\text{strong}} \approx \pi r_0^2$.

where r_0 is the phase coherence length scale defined such that $D_\phi(r_0) = 1$ rad. Kolmogorov turbulence, which describes how kinetic energy injected at an outer length scale r_{out} cascades to increasingly smaller scales until finally dissipated at an inner length scale r_{in} , predicts $\beta = 5/3$ in the domain $r_{\text{in}} \ll r \ll r_{\text{out}}$. This scaling has been demonstrated to be a reasonable approximation for the ISM over scales $r \sim 10^2$ km to > 1 AU [24], and also for the troposphere with $r < \Delta h$, where Δh is the thickness of the turbulent layer [11]. The specifics of the tropospheric model will be explored further in later sections.

The two length scales, r_F and r_0 , define the nature of the scattering which is split into the strong and weak regimes, Fig. reffig:scatter. In weak scattering, $r_0 \gg r_F$ and hence by equation 2.6, $D_\phi(r_F) \ll 1$. This implies that most of the radiative power measured on a point \mathbf{X} will originate from a screen area $A_{\text{weak}} \approx \pi r_F^2$. Whereas in the regime of *strong scattering*, $r_0 \ll r_F$ yielding $D_\phi(r_F) \gg 1$. This results in coherent signal propagation onto the point \mathbf{X} from multiple disconnected zones each of area $A_{\text{strong}} \approx \pi r_0^2$ [31]. Scattering in the troposphere and ISM fall into the regimes of weak and strong scattering respectively.

To evolve the screen in time, we assume a frozen screen i.e. that the velocity of the individual turbulent eddies is dominated by the bulk motion of scattering medium [e.g. 27]. This allows us to treat the screen as frozen but advected over the observer by a constant motion. Hence time variability can be easily incorporated by the relative motion between source, scattering screen and observer.

Table 2.1: A re-analysis of VLBI observations of Sgr A* by [?] has yielded revised estimates of the parameters associated with the Gaussian scattering kernel. An accurate estimation is needed for accurate extrapolation to 1.3 mm. Note that the position angle is measured East of North.

| | | |
|---|------|------|
| major axis FWHM (mas/cm ⁻²) | 1.32 | 0.04 |
| minor axis FWHM (mas/cm ⁻²) | 0.82 | 0.21 |
| position angle (°) | 77.8 | 9.7 |

2.2 Interstellar medium scattering

Electron density inhomogeneities in the interstellar medium (ISM) plasma scatter the radio emission from the Galactic centre. Radio interferometric observations of Sgr A* have characterised the basic properties of the intervening plasma material, however extensive developments in scattering theory and simulations have proved essential to the interpretation of more subtle scattering phenomena. This section begins with the early observational results which studied the Gaussian blurring effect of the scattering; we then expand on the scattering theory introduced in Sec. 2.1.1 to review the latest theoretical developments which explore the presence of scattering-induced substructure; finally we review recent observational results which account for scattering substructure in their data interpretation.

The dominant observational effect of the scattering for $\lambda \gtrsim$ cm is to convolve the intrinsic source structure with an elliptical Gaussian. The size of the Gaussian exhibits a λ^2 scaling dependence over several orders of magnitude [Fig. 2.2 ? ? 5?], which is consistent with the wavelength dependence of the refractive index of a plasma. In order to determine the parameters of the scattering kernel, i.e. major axis, minor axis and position angle, one has to observe at wavelengths where the angular size of scattering ellipse is much larger than the expected source size. A Very Long Baseline Array (VLBA) + Green Bank Telescope (GBT) campaign [5] estimated the size at 1.31×0.64 mas cm⁻², oriented 78° east of north.

An accurate extrapolation of scattering kernel to 1.3 mm is important for the EHT scattering-mitigation strategy [18] which aims to deblur the scattered image through a deconvolution procedure. However as this extrapolation is over at least an order of magnitude, any small systematic error in the original measurement can significantly effect the 1.3 mm extrapolated parameters. A recent review of VLBI observations of Sgr A* [?] has noted that there are significant inconsistencies between different measurements. The authors used a Bayesian methodology to re-analyse the datasets resulting in increased uncertainties as shown in 2.1. The minor axis has a much larger uncertainty than the major axis due to the limited north-south coverage of the VLBA.

The Gaussian blurring effect can explained by the simple scattering model introduced in Sec. 2.1.1. Recall, that in the strong scattering regime light is propagated from coherent patches with linear size $\sim r_0$. Each patch will emit light coherently into a single-slit diffraction cone of angular size $\theta_{\text{scatt}} \sim \lambda/r_0$. An observer will hence be illuminated by many patches spanning θ_{scatt} , yielding a blurred and broadened image, with projected size on the screen equal to the

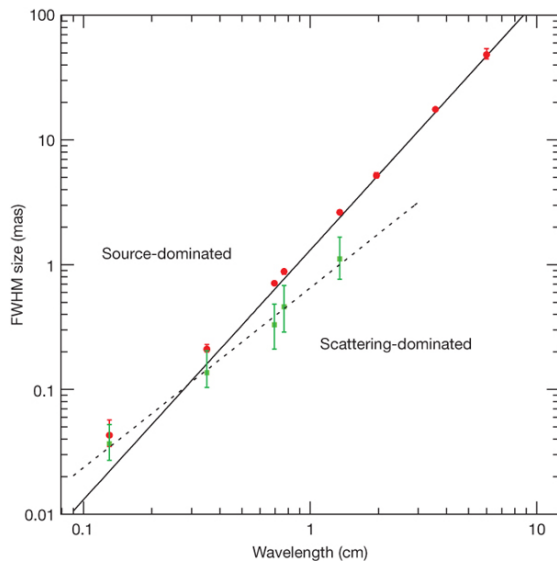


Figure 2.2: The λ^2 dependence of scattering kernel size is shown by the solid line. This has been derived from measurements made at $\lambda > 17$ cm [5]. The dotted line shows the derived intrinsic source size which scales as $\lambda^{1.44}$. This was derived from measurements in the wavelength range, $2 \text{ cm} < \lambda < 1.3 \text{ mm}$. The red circles show major-axis observed sizes of Sgr A* and the green points show the derived intrinsic major-axis size. This plot was reproduced from (author?) [15].

refractive scale

$$r_{\text{ref}} = \theta_{\text{scatt}} D_{\text{os}} = r_F^2 / r_0.$$

r_{ref} is the third fundamental length scale in the strong scattering regime and is associated with the refractive timescale,

$$t_{\text{ref}} = r_{\text{ref}} / v.$$

We can calculate r_0 given the FWHM of θ_{scatt} through the more precise relation

$$\theta_{\text{scatt}} = \frac{2\sqrt{2 \ln 2}}{2\pi} \lambda / r_0 (M + 1) \quad (2.7)$$

where $M = D_{\text{os}} / R$ is the magnification and R is the source-screen distance. The magnification factor is a correction to the model introduced in Sec. 2.1.1 when $R \sim \infty$ no longer holds and should be used when calculating distances in the observer plane [19]. The location of the scattering medium was originally thought to be quite close to Sgr A*. However, observations of a newly discovered pulsar, SGR J1745-29, indicate that the scattering screen is located at a distance $D_{\text{os}} = 5.8 \pm 0.3$ kpc, within the Scutum spiral arm. Using Eq. 2.7 and the parameters given in table 2.1, we find that the major axis of the coherence length at 1.3 mm, $r_0 \approx 3136.67$ km.

As the VLBI moves to higher frequencies, focus has shifted away from the well-studied Gaussian convolution effect of ISM scattering and onto the presence of stochastic scattering-induced substructure. To understand this phenomenon, we must first develop our conceptual framework.

Strong scattering can be further subdivided into *snapshot*, *average* and *ensemble-average* regimes [32, 19]. To understand the different regimes, remember that for each point on the source, the observer sees emission from coherent patches of size $\sim r_0$ spanning $\sim r_{\text{ref}}$. The diffraction cones from each of the patches will interfere, resulting in a multi-slit *diffractive scintillation* pattern.

In the *snapshot regime*, a compact source is observed with a narrow bandwidth and over a short time integration. This yields a single realisation of the diffractive scintillation pattern. By averaging over many snapshots, diffractive scintillation is quenched. This occurs if the source size θ_{src} is much larger than the diffractive scale $\theta_{\text{src}} \gg r_0 / R$; if the fractional bandwidth $\delta\nu / \nu$ is much larger than the decorrelation bandwidth $\delta\nu / \nu \gg \delta\nu_{\text{dc}} / \nu \approx (r_0 / r_F)^2$ [31]; or if the integration time t_{int} is much larger the diffractive timescale $t_{\text{int}} \gg t_0 = r_0 / v$, where v is the relative velocity between screen, source and observer. This regime is hence only accessible through observations of compact objects like pulsars. On a side note, observations in this regime can be used to probe the source with angular resolution given by the $\sim \lambda / r_{\text{ref}}$ [e.g. ?]. This is because the scattering screen is essentially a lens of size $\approx r_{\text{ref}}$.

In the *average regime*, diffractive scintillation has been averaged over, however there still exists scintillation over scales comparable to the size of the scattered image of a point source $\sim r_{\text{ref}}$, termed *refractive scintillation*. Phase fluctuations on this scale acts like a weak lens to focus or defocus the λ / r_0 scale diffraction cones in the direction of the observer. For a point source this would lead to weak flux variations in the total flux [31]. We will show later that refractive scintillation leads to the presence of substructure for a resolved scatter-broadened source. In contrast to diffractive scintillation, refractive scintillation is much more difficult to average over. Typically the refractive time

scale $t_{\text{ref}} = r_{\text{ref}}/v$ is on the order of weeks to months for Sgr A*; the fractional decorrelation bandwidth is on the order of unity $\delta\nu_{\text{dc}}/\nu \sim 1$; and the source has to be much larger than the image of a scattered point source $\theta_{\text{src}} \gg \theta_{\text{scatt}}$.

In the *ensemble-average regime*, both diffractive and refractive scintillation have been averaged over. It is in this regime when the scattering is equivalent to Gaussian convolution which is deterministic and not time variable.

A recent theoretical work [24] has derived a useful approximation of the resolved scattered image I_{ss} in the average regime,

$$I_{\text{ss}}(\mathbf{x}) \approx I_{\text{src}}(\mathbf{x} + r_F^2 \nabla \phi(\mathbf{x})), \quad (2.8)$$

where ∇ is the directional derivative. Here we have used the same two-dimensional coordinate system, indexed by \mathbf{x} to describe the source, screen and observer planes which are considered to be aligned along the vertical axis. The scattered image I_{ss} is approximated by a 'reshuffling' of the source image I_{src} . As $|\nabla\phi| \sim 1/r_0$, the magnitude of the translation of points on $I_{\text{src}} \sim r_{\text{ref}}$.

Even though $\phi(\mathbf{x})$ is only coherent to $\sim r_0$, the directional phase derivative $\nabla\phi(\mathbf{x})$ remains spatially coherent over much larger scales. Following (**author?**) [24], the autocovariance of phase derivative can be related to the structure function

$$\langle [\partial_x \phi(\mathbf{x}_0)][\partial_x \phi(\mathbf{x}_0 + \mathbf{x})] \rangle = -\partial_x^2 \langle \phi(\mathbf{x}_0) \phi(\mathbf{x}_0 + \mathbf{x}) \rangle \quad (2.9)$$

$$= \partial_x^2 D_\phi(\mathbf{x}). \quad (2.10)$$

Using a typical structure function [?], We are interested in the case $r_{\text{in}} \gg r_0$, the structure function becomes [?]

$$D_\phi = \begin{cases} \left(\frac{r}{r_0}\right)^2 & \text{if } r \ll r_{\text{in}}, \\ \frac{2}{\beta} \left(\frac{r_{\text{in}}}{r_0}\right)^{2-\beta} \left(\frac{r}{r_0}\right)^\beta & \text{if } r \gg r_{\text{in}}. \end{cases}$$

Hence We are interested in the case r/ggr_{in}

$$\partial_x^2 D_\phi(\mathbf{x}) = \left(\frac{r_{\text{in}}}{r_0}\right)^{2-\beta} 2(\beta-1) \frac{r^{\beta-2}}{r_0^\beta} \quad (2.11)$$

We now investigate the coherence of Image shift relative to the refractive scale,

PLOT

moves pixels arounds by refractive scale 10 uas If $\nabla\phi(\mathbf{x})$ was incoherent between patches of size $\sim r_0$, this would effectively be convolution with Gaussian of size r_{ref} .)

Recent observations have revealed flux modulation due to scattering substructure ~ 10 mJy at 1.3 cm [see Fig. reffig:substructure1 20] as well as non-zero closure phases at 3.5 mm [see Fig. reffig:substructure2 ?].

Observations at mm-wavelengths have revealed deviations from the λ^2 scaling law, see Fig. 2.2. This is interpreted as due to the presence of intrinsic source structure and has been fitted with a power-law with an exponent of 1.34 ± 0.01 [?]. This has enabled the constraint of various theoretical models [5], excluding advection-dominated accretion flows (ADAF) [?] and Bondi-Hoyle accretion [?]. However observations extending over month timescales are required to

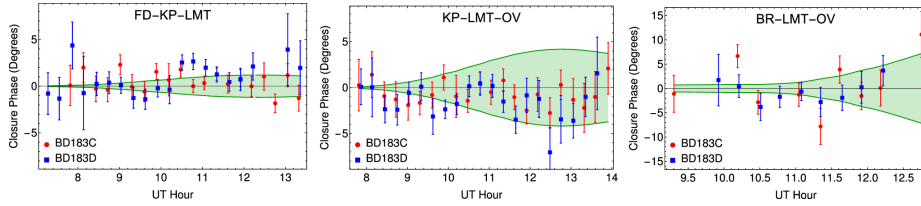


Figure 2.3: Closure phases recorded in a VLBA + LMT observation of Sgr A* at $\lambda = 3.5$ mm [?]. The data points are shown as red circles and blue squares and are only distinguished by the calibrator used. The green envelopes show the 1σ closure phase prediction induced by scattering-induced substructure. Reproduced from ?]

properly sample the larger scale inhomogeneities and even with multiple epoch observations, it can be difficult to distinguish source and scattering characteristics [?].

Narayan Goodman (1989; hereafter NG89) and Goodman Narayan (1989; hereafter GN89) demonstrated that the refractive contribution to noise, which arises from substructure within the scattering disk, can dominate measurements on such long baselines. Moreover, this noise can be easily decoupled from intrinsic variability and can provide information about the source and scattering properties without sampling a refractive ensemble. It therefore provides a robust and rapid mechanism for quantifying refractive effects

Structure function goes quadratic at small scales then kolmogorov then constant (Tatarskii, 1971).

2.3 Troposphere

The coherence and intensity of millimetre wavelength electromagnetic waves are most severely deteriorated in the lowest atmospheric layer, the troposphere, which extends up to an altitude of 7 – 10 km above sea level and down to a temperature $T \sim 218$ K [45]. The troposphere is composed of primary gases N₂ and O₂, trace gases e.g. water vapour and CO₂, as well as particulates of water droplets and dust.

2.3.1 Propagation through a linear medium

Consider a quasi-monochromatic wave passing through a linear medium,

$$E(x, t) = E_0 \exp^{i(knx - 2\pi\nu t)}, \quad (2.12)$$

where k is the propagation constant in free space equal to $2\pi\nu/c$ and n is the complex index of refraction, $n = n_R + jn_I$. If n_I is nonzero the wave will decay exponentially. The linear absorption coefficient or fraction of power absorbed per unit length traversing the medium is defined as

$$\kappa_\nu = 4\pi\nu n_I/c. \quad (2.13)$$

The phase velocity of light slows according to the refractive index, $v_p = c/n_R$,

which results in a time delay. Because the electric field is causal, n_R and n_I contain the same information and can be interchanged via the Kramers-Kronig relations. The time delay, δt and optical depth τ can be calculated in general,

$$\delta t + i\tau = 1/c \int_{medium} d^3\mathbf{x} (n(\mathbf{x}, \nu) - 1), \quad (2.14)$$

where the integral is over the total path through the medium.

Absorption is accompanied by emission and for a medium in local thermodynamic equilibrium, Kirchoff's law states that

$$\frac{\epsilon_\nu}{\kappa_\nu} = B_\nu(T), \quad (2.15)$$

where $\epsilon_\nu = dI_\nu/dx$ is the macroscopic emission coefficient and $B_\nu(T)$ is the Planck function. Hence the absorbing molecules are also emitters, increasing system noise.

2.3.2 Average atmosphere

We start from the unpolarised radiative transfer equation, which is unidirectional in the absence of scattering,

$$\frac{dI_\nu(s)}{ds} = \epsilon_\nu(s) - \kappa_\nu(s)I_\nu(s), \quad (2.16)$$

where s is the coordinate along the signal path through the atmosphere, $I_\nu(s)$ is the specific intensity, ϵ_ν is the macroscopic emission coefficient and κ_ν is the macroscopic absorption coefficient. The assumption of local thermodynamic equilibrium (LTE) holds as the collisional timescale is much smaller than the time for spontaneous emission up to altitudes ≥ 80 km after which there is only $\sim 0.001\%$ of mass left. (Pardo et al., ibid) Using Kirchoff's law, equation 2.15, multiplying by $\exp(-\tau_\nu)$ and integrating yields,

$$I_\nu(s) = I_\nu(0)e^{-\tau_\nu(0,s)} + \int_0^s B_\nu(s')e^{-\tau_\nu(s',s)}\kappa_\nu(s')ds' \quad (2.17)$$

where s' is a dummy variable in the same direction as s and $\tau_\nu(0,s) = \int_0^s k_\nu(s')ds'$. $I_\nu(0)$ is taken as the radiance from the cosmic background.

The above equation will allow us to calculate the noise temperature of the atmosphere by converting the output radiance at the ground $I_\nu(s)$ to the equivalent blackbody temperature through inversion the Planck function. To calculate the opacity and complete the above integral, κ_ν needs to be calculated over the frequency range. Note again that ϵ can easily be calculated from κ , and vice-versa, using Kirchoff's law. The mean time delay can be calculated using the Kramers-Kronig relations. The fluctuations in time delay will be given in section ?? .

The absorption spectrum in the GHz range (e.g. (author?) 36) is dominated by several transitions of H_2O and O_2 as well as a pseudo-continuum opacity which increases with frequency. The pseudo-continuum opacity is due to the far wings of a multitude of broadened water vapour lines above 1 THz [9].

A general equation of the absorption coefficient for a transition between a lower l and upper u states is given in the original paper. Here we merely point out that it should be proportional to the energy of the photon, $h\nu_{l \rightarrow u}$, the transition probability or Einstein coefficient, $B_{l \rightarrow u}$, the line-shape, $f(\nu, \nu_{l \rightarrow u})$ and the number densities N of electronic populations. Line profiles which describe pressure broadening (perturbations to the Hamiltonian due to the presence of nearby molecules) and Doppler broadening are used. The condition of detailed balance further requires that decays from the upper state are included yielding, $g_u B_{u \rightarrow l} = g_l B_{l \rightarrow u}$, where g is the degeneracy of the electronic state. Putting this together we find,

$$\kappa(\nu)_{l \rightarrow u} \propto h\nu B_{l \rightarrow u} \left(\frac{N_l}{g_l} - \frac{N_u}{g_u} \right) f(\nu, \nu_{l \rightarrow u}), \quad (2.18)$$

where the Einstein coefficients are calculated from the inner product of the initial and final states with the dipole transition operator. The number densities of the two states, N_u and N_l in local thermodynamic equilibrium (LTE) are simply related to the local number density and temperature via Boltzmann statistics.

Assuming LTE, the electron population energy level depends only on the local temperature, $T(s)$ and density of the i th species $N_i(s)$. To perform the numerical integration, the atmosphere is discretised into layers of variable thickness with an accuracy ~ 0.1 K. Temperature & density profiles are calculated based on several station dependent inputs to the API, namely, ground temperature & pressure, precipital water vapor content (PWV), altitude scale height of water vapour and the troposphere lapse rate.

Radiative transfer is applied to each absorption line through a sum over each atmospheric layer, chemical species and transition line,

$$\tau_\nu = \sum_{i(layers)} \left[\sum_{j(molec.)} \left(\sum_{k(lines)} \kappa_{\nu,k} \right)_j \right]_i \cdot \Delta s_i \quad (2.19)$$

where Δs_i is the path through the homogenous i th layer.

A general equation of the absorption coefficient for an arbitrary line transition $\kappa(\nu)_{l \rightarrow u}$ is given in the original paper. Here I merely note that it is proportional to the energy of the photon, $h\nu_{l \rightarrow u}$, the transition probability or Einstein coefficient, $B_{l \rightarrow u}$ and the lineshape, $f(\nu, \nu_{l \rightarrow u})$. The condition of detailed balance requires that decays from the upper state are included yielding, $g_u B_{u \rightarrow l} = g_l B_{l \rightarrow u}$. Putting this together we have the proportionality,

$$\kappa(\nu)_{l \rightarrow u} \propto h\nu B_{l \rightarrow u} \left(\frac{N_l}{g_l} - \frac{N_u}{g_u} \right) f(\nu, \nu_{l \rightarrow u}). \quad (2.20)$$

Physically, the lineshape originates from perturbations to the hamiltonian due to proximity to neighbouring molecules, called pressure broadening, and at lower pressures, thermal doppler broadening. A Van Vleck -Weisskopf (VVW) profile is used for pressure broadening. At lower pressures this is convolved with a gaussian which arises from the Maxwellian distribution. The population densities in LTE are given by boltzmann distribution

$$\frac{N_n}{N} = g_n \frac{\exp -\frac{E_n}{kT}}{Q} \quad (2.21)$$

where Q is the partition function. $Q = \sum_i g_i \exp -E_n/kT$. The Einstein absorption coefficients are calculated using

$$B_{l \rightarrow u} = \frac{2\pi}{3\hbar^2} | \langle u | \mu | l \rangle |^2, \quad (2.22)$$

where $|u\rangle$, $|l\rangle$, $|\mu\rangle$ are the wavefunctions of upper and lower states and the dipole transition operator respectively.

Transition lines at radio wavelengths result from rotational state transitions. To calculate the inner product given in equation 2.22, hamiltonians for linearly symmetric rotors (e.g. O_2 , CO) and asymmetric rotors are used. The asymmetric rotations are decomposed into three principal rotation axes with differing rotational constants governing each axis. Rotational constants were measured by the authors as well as drawn from a variety of literature. Partition functions and transition probability are calculated using approximations taken from the literature.

Far wing broadening of H_2O lines > 1.2 THz extends to lower frequencies and is not completely represented by the VVW profile. This is believed to be due to self-self collisions of water molecules. Additionally there are terms from the dry atmosphere related to transient dipoles and Debye absorption which are not represented in the lineshape. To correct for these effects two pseudocontinua are used. This takes the form of a power law dependence on ν, T , and the molecular densities. The parameters involved in the pseudocontinua as well as a subset of the rotational constants are based on Fourier transform spectroscopy measurements on Mauna Kea which was used to refine and test the model.

2.3.3 Turbulent atmosphere

In contrast to the other atmospheric chemical components, water vapour mixes poorly and its time-variable spatial distribution induces rapid fluctuations in the measured visibility phase at short wavelengths. The water vapour column density is measured as the depth of the column when converted to the liquid phase and is referred to as the precipitable water vapour (PWV). The PWV is, via the real component of the refractive index, directly proportional to phase offset,

$$\delta\phi \approx \frac{12.6\pi}{\lambda} \times w, \quad (2.23)$$

where w is the depth of the PWV column [9] and an atmospheric temperature $T = 270$ K has been assumed. This relationship between phase and water vapour content has been experimentally verified [22]. At 230 GHz, the change in PWV needed to offset the phase by 1 rad is $\Delta w \approx 0.03$ mm. This sensitive dependence of phase coherence on atmospheric stability is aggravated by typically low antenna observation elevation angles, uncorrelated atmospheric variations between stations, and observing with a sparse VLBI array.

Visibility phase instability $\delta\phi(t)$ due to tropospheric turbulence is a fundamental limitation to producing high fidelity, science-quality maps with a mm-VLBI array [45]. The coherence time-scale is typically too rapid ($\lesssim 10$ s) for

fast switching calibration, so other calibration procedures (e.g. water vapour radiometry, paired antennas, sub-arrays, and/or self-calibration) must be used. Self-calibration is the most commonly used but is limited by the integration time needed to obtain adequate SNR to fringe fit. This often leads to the use of closure quantities to perform model fitting ((author?) 13; (author?) 16).

The shifting distribution of water vapour in the troposphere causes the refractive index and hence the phase velocity to change on timescales of seconds and of spatial scales of metres (Thompson et al., *ibid*). At centimeter wavelengths and below, water vapour in the troposphere dominates errors in delay and delay rate over hydrogen maser clock errors (Rogers & Moran, 1981). Stochastic phase errors lead to a decrease in flux due to incoherent vector averaging. This makes it difficult to obtain adequate SNR for calibration. The uncertainty in the phase degrades structural information which makes conventional imaging difficult and hence closure quantities are often used (e.g. Fish et al 2011). Incoherent phases represent a fundamental limit to all types of interferometry. Figure ?? gives a cartoon illustration of the shifting distribution of water vapour above a baseline.

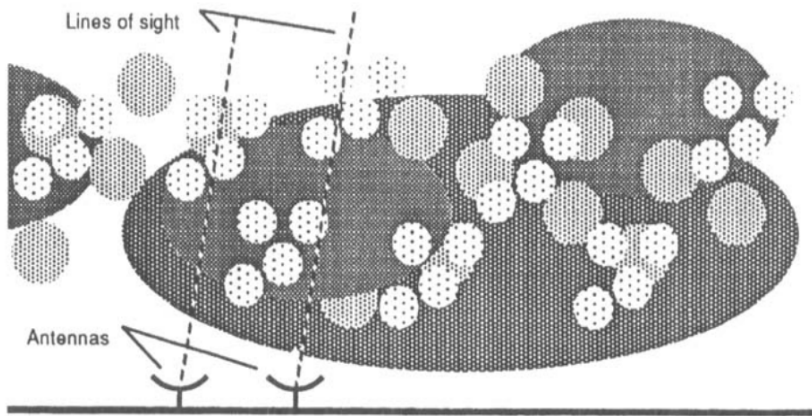


Figure 2.4: A cartoon illustration of poorly mixed water vapour moving over a baseline (credit : Thompson et al, *ibid*)

2.3.4 Instrumental

Thermal Noise

Does this properly take into account individual antenna noises that are correlated? Unexpectedly this implementation becomes important for the non-zero trop cp later.

Antenna Pointing

All antennas suffer pointing errors to some degree due to a variety of factors including dish flexure due to gravity, wind and thermal loading, as well as drive

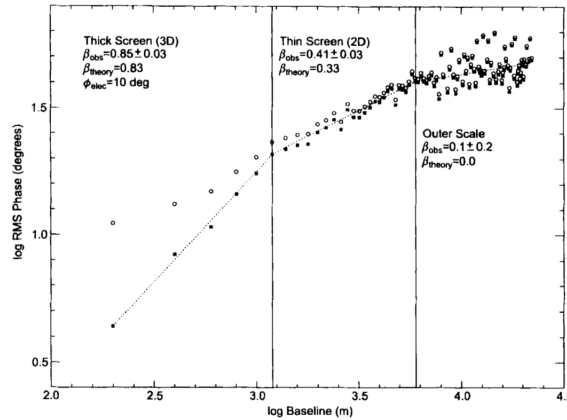


Figure 2.5: showing β changes with distance on the phase screen. Note the three distinct regime but continuous variation in between

mechanics. This corresponds to an offset primary beam, which should only translate to minor amplitude errors if the pointing error θ_{PE} is significantly smaller than the primary beam (i.e. $\theta_{\text{PE}} \ll \theta_{\text{PB}}$). In the Measurement Equation formalism, this offset can be represented by a modified (shifted) primary beam pattern in the E -Jones term

$$\mathbf{E}_p(l, m) = \mathbf{E}(l_0 + \delta l_p, m_0 + \delta m_p), \quad (2.24)$$

where $\delta l_p, \delta m_p$ correspond to the directional cosine offsets.

We investigate the effect of pointing errors on the 50 m (i.e. fully illuminated) LMT dish configured in an eight station VLBI array. The LMT has been measured to have an absolute pointing accuracy of $\sigma_{\text{abs}} = 1 - 3$ arcsec, where smaller offsets occur when observing sources closer to zenith, and a tracking pointing accuracy $\sigma_{\text{track}} < 1$ arcsec¹. We explore the observational effect of these errors through three different pointing error models which explore different instructive and plausible scenarios. The LMT has been singled out as this may well serve as a reference station for the EHT array given its sensitivity and central geographic location. The source used is a circular Gaussian of characteristic size $\Theta_{\text{src}} = 50 \mu\text{-arcsec}$, located at the phase centre. For this investigation, as long as $\Theta_{\text{src}} \ll \theta_{\text{PB}}$, the exact structure of the source is unimportant. We approximate the LMT beam profile using an analytic WSRT beam model [37] with a factor of 2 increase in the beam factor C to take into account the increased dish size

$$E(l, m) = \cos^3(C\nu\rho), \quad \rho = \sqrt{\delta l_p^2 + \delta m_p^2} \quad (2.25)$$

where C is a constant, with value $C \approx 130 \text{ GHz}^{-1}$. Note that the power beam EE^H becomes \cos^6 , giving a FWHM = 6.5 arcsec. In Fig. 4.5, we show this for pointing accuracies spanning the range from $\rho \sim 0 - 4.5$ arcsec.

In the first case we assume a constant pointing error and plot the RMS relative visibility amplitude error $\sigma_{\Delta V/V_0}$ on baselines to LMT, where $\Delta V = V_{\text{point}} - V_0$, V_{point} and V_0 are the amplitude of the visibility with and without

¹<http://www.lmtgtm.org/telescope/telescope-description/>

pointing errors respectively. This simulation is meant to be instructive as to the typical amplitude error in the simplest possible scenario.

Also interesting to consider is a slower, continuous time-variable pointing error associated with the tracking error σ_{track} . Physically this could be attributed to changes in wind, thermal and gravitational loading which all change with telescope pointing direction and over the course of a typical few hour observation. Using the MeqTrees software package, such behaviour has been demonstrated to occur with the Westerbork Synthesis Radio Telescope (WSRT, [44])². This is modeled as a sinusoid with period sampled from a uniform distribution between 0.5 and 6 hours, and a peak amplitude $A_\rho = \sqrt{2}\sigma_\rho$, where the factor $\sqrt{2}$ relates the amplitude to the RMS for periodic zero mean waveforms.

Whilst a stationary phase centre is tracked, the pointing error should evolve slowly and smoothly, however, in mm-VLBI observations the phase centre is often shifted to another source/calibrator. This would cause the pointing error to change abruptly, with an absolute pointing error σ_{abs} . Source/calibrator change is scheduled every 5-10 minutes in a typical millimetre observation. The point is that even though EHT will be able to determine the pointing offset when observing a calibrator with well known structure, when the antennas slew back to a source (e.g. Sgr A*) with less certain or variable source structure, the pointing error could change significantly. This is exacerbated by the scarcity of mm-wavelength calibrators, which are often widely separated from the source. We simulate this effect by re-sampling the pointing error every 10 minutes from a Gaussian of characteristic width equal to the quoted pointing error. We perform 50 realisations of the simulation for each pointing offset to generate reasonable uncertainties.

Polarisation

²See also <https://indico.skatelescope.org/event/171/session/9/contribution/20>

Chapter 3

Software architecture and implementation

3.1 Simulator

MEQSILHOUETTE is an observation and signal corruption simulator written in PYTHON and MEQTREES using the MEASUREMENT SET¹ data format. A flow diagram of the simulator is shown in Fig. 3.1. Input to the simulator is a sky model and configuration file. The former is typically a time-ordered list of FITS images, where each image represents the source total intensity² over a time interval $\Delta t_{\text{src}} = t_{\text{obs}}/N_{\text{src}}$, where t_{obs} is the observation length and N_{src} is the number of source images. The configuration file specifies all parameters needed by the pipeline to determine the particular observation configuration (array, frequency, bandwidth, start time, etc) and which signal corruption implementation should be employed. The primary outputs of the pipeline are an interferometric dataset in MEASUREMENT SET format along with the closure phases and uncertainties and a dirty and/or cleaned image. The modular structure of the pipeline allows for multiple imaging and deconvolution algorithms to be employed. The rest of this section is devoted to describing the implementation of each signal corruption module.

This section details the software architecture used for the simulation code as well as the RODRIGUES online interface. It will refer back to the signal corruption and simulation theory sections as well as the code itself. Furthermore the code has been written with the intention of being readable, hence minimum comments needed. This has hopefully been achieved through keeping to the logical flow underlying the code and explanatory names. The highest level or driver script is written in Python which interfaces easily with other systems. The bulk of the computational load is called through other programs, written in C++ which are faster. The CASA Measurement Set(MS) is data format of choice, although in the mm-VLBI field other formats are currently still more popular i.e. UVFITS or HOPS but with the rise of ALMA, the MS format will inevitably become the next generator data format and already is used at JIVE.

¹<https://casa.nrao.edu/Memos/229.html>

²Later versions of MEQSILHOUETTE will enable the full Stokes cubes as input.

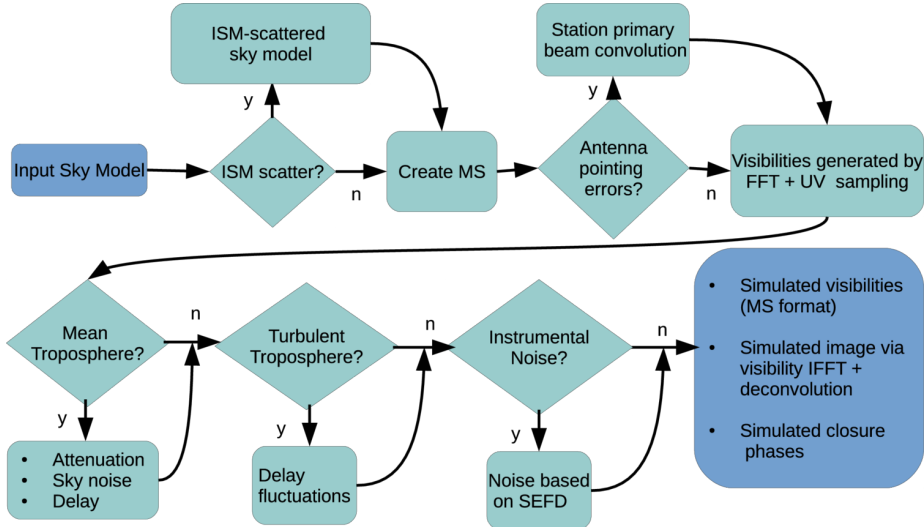


Figure 3.1: Flow diagram showing basic sequence of the MEQSILHOUETTE simulation pipeline. The sky model could include (a) a time-ordered list of FITS images or (b) parametric source model consisting of Gaussians or point sources. The details of the station information, observation strategy, tropospheric and ISM conditions are specified in a user-defined input configuration file. The pipeline is flexible, allowing any additional, arbitrary Jones matrices to be incorporated. Further details in text.

from source variability: To test these effects, we include time variability for source in meqs. A discussion of calibration and interpretation of time variability, including separating out time-variable and quiescent structure is outside the scope of this thesis, but hopefully mm-VLBI can use some techniques from other time-variable domains of interferometry like pulsar searches or scintillation analyses.

3.1.1 ScatterBrane

The turbulent phase screen $\phi(\mathbf{x})$ can be generated from the phase spatial power spectrum (see Appendix C (**author?**) [24]).

Scattering in the ISM at millimetre wavelengths falls into the strong scattering regime, which has been quantitatively described in the literature [32, 19] and implemented in the PYTHON-based SCATTERBRANE³ package, based on (**author?**) [24]. This approach extends the turbulent model described in section 2.1.1 to regimes where the inner and outer turbulent scales as well as the anisotropy of scattering kernel are considered. The distance to the screen is taken from the best-fit solution from (**author?**) [4] and is located, not at the Galactic Centre, but rather in the Scutum spiral arm at a distance $D_{\text{os}} = 5.8 \pm 0.3$ kpc.

We aim to place this description of ISM scattering, which has already yielded an important context for mm-VLBI observation [e.g. 35], into a broader simula-

³<http://krosenfeld.github.io/scatterbrane/current>

tion framework. Our ISM module uses the public SCATTERBRANE code together with an interfacing task which ensures adequate time resolution for sampling ISM variability. If the time resolutions chosen to sample the source variability Δt_{src} and screen variability Δt_{ism} are unequal, we set

- $\Delta t_{\text{ism}} = \Delta t_{\text{src}}$ if $\Delta t_{\text{src}} < \Delta t_{\text{ism}}$
- $\Delta t_{\text{ism}} = R(\frac{\Delta t_{\text{src}}}{\Delta t_{\text{ism}}})\Delta t_{\text{src}}$ if $\Delta t_{\text{src}} > \Delta t_{\text{ism}}$,

where R rounds the fraction to the nearest integer.

3.1.2 Atmospheric

The problem of radiative transfer through a static atmosphere is well described and implemented by the Atmospheric Transmission at Microwaves (ATM) package [36]. ATM has been incorporated into MEQSILHOUETTE to provide a fast and sophisticated procedure to calculate average opacities, sky brightness temperatures and time delays. Here we provide a brief summary of the theory underpinning the package but see the original paper for further detail. ATM is commonly used in the ALMA community [12, 33] and has been tested with atmospheric transmission spectra taken on Mauna Kea [41].

The goal is to integrate this equation over the signal path which requires κ_ν as a function of altitude and frequency. In practice, this involves a triple sum over altitude layer, chemical species and rotational energy transition. Atmospheric temperature and pressure profiles are calculated based on several station dependent inputs, namely, ground temperature and pressure and the precipitable water vapour column depth.

Typical opacities and sky brightness temperatures for ALMA, Submillimeter Array (SMA) and SPT are shown in Fig. 4.2. A typical PWV range [25], ground pressure and temperature were assumed for each site. Note that both the opacity and brightness temperature are inversely proportional to the ground temperature and proportional to ground pressure.

Following from section 2.1.1, we can model the statistics of $\delta\phi(t)$ with a thin, frozen, Kolomogorov-turbulent phase screen moving with a bulk velocity, v . We set the height h of the screen at the water vapour scale height of 2 km above ground. We will show later that the thickness Δh of the atmospheric turbulent layer can be neglected in our implementation. At 1.3 mm, the Fresnel scale is $r_F \approx 0.45$ m and experiments show annual variations of $r_0 \sim 50 - 500$ m above Mauna Kea [29] and $r_0 \sim 90 - 700$ m above Chajnantor [39], where both sites are considered to have excellent atmospheric conditions for millimetre astronomy. As $r_F < r_0$, this is an example of weak scattering.

The required field-of-view (FoV) of a global mm-VLBI array is typically $\text{FoV} < 1$ mas or $\sim 10 \mu\text{m}$ at a height of 2 km, which is roughly 7-8 orders of magnitude smaller than the tropospheric coherence length. The tropospheric corruption can therefore be considered constant across the FoV and, from the perspective of the Measurement Equation, modeled as a diagonal Jones matrix per time step. As VLBI baselines are much longer than the coherence length, $|\mathbf{b}| \geq 1000$ km $>> r_0$, the phase screen at each site must be simulated independently.

Our aim then is to produce a phase error time sequence $\{\delta\phi(t_i)\}$ for each station which is added to the visibility phase. We invoke the frozen screen

assumption and write the structure function as a function of time, $D(t) = D(r)|_{r=vt}$. The temporal structure function provides an efficient route to sample the variability of the troposphere at the integration time of the dataset, $t_{\text{int}} \sim 1$ sec. This definition is only applicable in the regime $r > r_F$ to ensure diffraction effects are negligible [45].

The temporal variance of the phase is consequently a function of the temporal structure function, [46]

$$\sigma_\phi^2(t_{\text{int}}) = (1/t_{\text{int}})^2 \int_0^{t_{\text{int}}} (t_{\text{int}} - t) D_\phi(t) dt. \quad (3.1)$$

Assuming power-law turbulence and integrating yields,

$$\sigma_\phi^2(t_{\text{int}}) = \left[\frac{1}{\sin \theta(\beta^2 + 3\beta + 2)} \right] \left(\frac{t_{\text{int}}}{t_0} \right)^\beta, \quad (3.2)$$

where $t_0 = r_0/v$ is the coherence time and $1/\sin \theta$ is the approximate airmass which arises as $D_\phi \propto w$. As $r \ll \Delta h$, where Δh is the thickness of the turbulent layer, an thin screen exponent of $\beta = 5/3$ is justified [46]. The phase error time-series takes the form of a Gaussian random walk per antenna. At mm-wavelengths, the spectrum of water vapour is non-dispersive up to a few percent [12] and so we can assume a simple linear scaling across the bandwidth. Fig. 4.3 shows an example simulation of the turbulent and total delays at the SMA and ALMA sites.

Phase fluctuations $\delta\phi(t)$ can also simulated by taking the inverse Fourier transform of the spatial phase power spectrum. However this approach is much more computationally expensive, e.g. for an observation length t_{obs} involving $N_{\text{ant}} = 8$ independent antennae with dish radii $r_{\text{dish}} = 15$ m, wind speed $v = 10$ m s⁻¹ and pixel size equal to r_F , the number of pixels $N_{\text{pix}} \approx N_{\text{ant}} t_{\text{obs}} r_{\text{dish}}^2 / (v r_F^3) \sim 10^8$. Additionally, due to fractal nature of ideal Kolmogorov turbulence, the power spectrum becomes unbounded as the wavenumber approaches zero which makes it difficult to determine the sampling interval of the spatial power spectrum [26].

3.1.3 Pointing

We investigate the effect of pointing errors on the 50 m (i.e. fully illuminated) LMT dish configured in an eight station VLBI array. The LMT has been measured to have an absolute pointing accuracy of $\sigma_{\text{abs}} = 1-3$ arcsec, where smaller offsets occur when observing sources closer to zenith, and a tracking pointing accuracy $\sigma_{\text{track}} < 1$ arcsec⁴. We explore the observational effect of these errors through three different pointing error models which explore different instructive and plausible scenarios. The LMT has been singled out as this may well serve as a reference station for the EHT array given its sensitivity and central geographic location. The source used is a circular Gaussian of characteristic size $\Theta_{\text{src}} = 50 \mu\text{-arcsec}$, located at the phase centre. For this investigation, as long as $\Theta_{\text{src}} \ll \theta_{\text{PB}}$, the exact structure of the source is unimportant. We approximate the LMT beam profile using an analytic WSRT beam model [37] with a factor of 2 increase in the beam factor C to take into account the increased dish size

$$E(l, m) = \cos^3(C\nu\rho), \quad \rho = \sqrt{\delta l_p^2 + \delta m_p^2} \quad (3.3)$$

⁴<http://www.lmtgtm.org/telescope/telescope-description/>

where C is a constant, with value $C \approx 130 \text{ GHz}^{-1}$. Note that the power beam EE^H becomes \cos^6 , giving a FWHM = 6.5 arcsec. In Fig. 4.5, we show this for pointing accuracies spanning the range from $\rho \sim 0 - 4.5$ arcsec.

In the first case we assume a constant pointing error and plot the RMS relative visibility amplitude error $\sigma_{\Delta V/V_0}$ on baselines to LMT, where $\Delta V = V_{\text{point}} - V_0$, V_{point} and V_0 are the amplitude of the visibility with and without pointing errors respectively. This simulation is meant to be instructive as to the typical amplitude error in the simplest possible scenario.

Also interesting to consider is a slower, continuous time-variable pointing error associated with the tracking error σ_{track} . Physically this could be attributed to changes in wind, thermal and gravitational loading which all change with telescope pointing direction and over the course of a typical few hour observation. Using the MeqTrees software package, such behaviour has been demonstrated to occur with the Westerbork Synthesis Radio Telescope (WSRT, [44])⁵. This is modeled as a sinusoid with period sampled from a uniform distribution between 0.5 and 6 hours, and a peak amplitude $A_\rho = \sqrt{2}\sigma_\rho$, where the factor $\sqrt{2}$ relates the amplitude to the RMS for periodic zero mean waveforms.

Whilst a stationary phase centre is tracked, the pointing error should evolve slowly and smoothly, however, in mm-VLBI observations the phase centre is often shifted to another source/calibrator. This would cause the pointing error to change abruptly, with an absolute pointing error σ_{abs} . Source/calibrator change is scheduled every 5-10 minutes in a typical millimetre observation. The point is that even though EHT will be able to determine the pointing offset when observing a calibrator with well known structure, when the antennas slew back to a source (e.g. Sgr A*) with less certain or variable source structure, the pointing error could change significantly. This is exacerbated by the scarcity of mm-wavelength calibrators, which are often widely separated from the source. We simulate this effect by re-sampling the pointing error every 10 minutes from a Gaussian of characteristic width equal to the quoted pointing error. We perform 50 realisations of the simulation for each pointing offset to generate reasonable uncertainties.

3.1.4 RODRIGUES interface

For community use, we host the online, RODRIGUES, interface, found at <http://rodrigues.meqtrees.net/>. Each of the components of the simulator run in Docker containers. **Looks like the infrastructure is going to change, re: discussions with Gijs and Sphe, so going to wait before writing this.

3.2 Parameter estimation

⁵See also <https://indico.skatelescope.org/event/171/session/9/contribution/20>

Chapter 4

Results and analysis

4.0.1 Canonical simulations

Tropospheric induced closure phase errors !!A bug which came from averaging

In this paper, we present the first release of the MEQSILHOUETTE synthetic data simulation package. The pipeline is optimised towards mm-VLBI, taking into account user-specified stages of the signal propagation path, which enables the quantification of a range of systematic effects. Focus has been placed on modeling the effects of signal transmission through the ISM and troposphere as well as instrumental errors (i.e. pointing error and thermal noise). Time variability in all relevant domains (source, array, ISM, troposphere) is implemented. The run time for a typical simulation with a realistic instrumental setup is on the order of minutes. Implementation of polarisation effects is intended in the next release.

The ISM scattering implementation SCATTERBRANE, based on (**author?**) [24], has been incorporated into the pipeline. Fig. 4.1 provides an example of closure phase and flux variability over a 4 day period using a static source. Accurate simulation of the ISM-induced closure phase variation is essential in order to make any inference on asymmetric, event-horizon scale structure [e.g. 17, 35]. This will become even more important as the EHT sensitivity increases by an order of magnitude in the near future. Note that if the source has intrinsic spatial variability as in the case of a hotspot model [14], this will increase ISM variability as the relative motion between source, screen and observer is increased.

In section ??, we show how antenna pointing errors of the LMT could introduce fractional RMS amplitude variations $\sigma_{\Delta V/V_0} \leq 0.4$ on the timescale of phase centre switching. This would occur if the calibrator is widely separated from the source, as is often the case in mm-VLBI. In contrast tracking errors are less problematic with $\sigma_{\Delta V/V_0} \leq 0.05$. If the gain error is non-separable from the calibration model used, it could be interpreted as intrinsic variability, substructure and/or increased noise. If unaccounted for, this effect has the potential to limit the dynamic range of mm-VLBI images. Further tests to constrain the pointing uncertainties of EHT stations will lead to more accurate interferometric simulations and hence the overall impact on black hole shadow parameter estimation. Here we demonstrate the capability to incorporate a range of plausible pointing error effects into a full simulation pipeline.

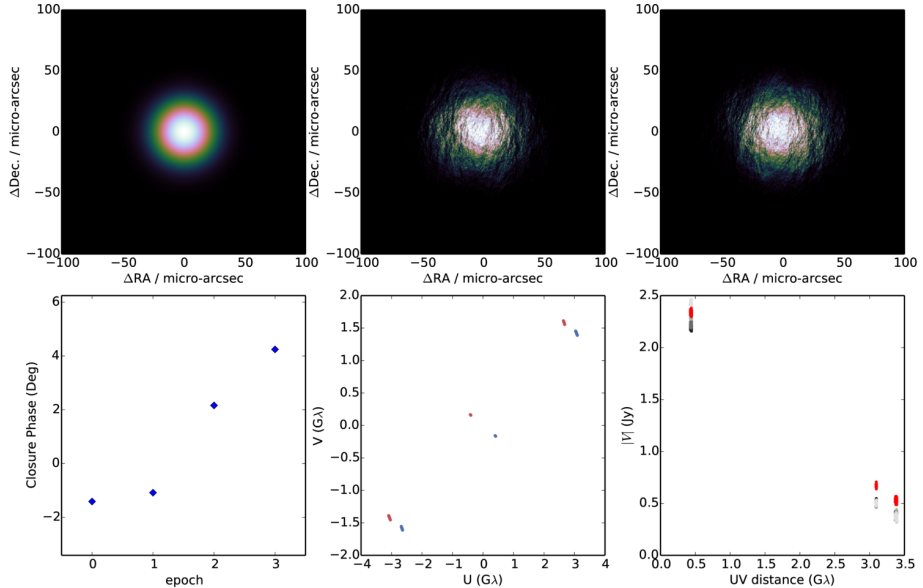


Figure 4.1: An example simulation of ISM scattering towards Sgr A*. The top panel, left to right, shows the original $\text{FWHM} = 40 \mu\text{-arcsec}$ Gaussian (**top left**), the ISM scattered image on the first night (**top middle**) and last night (**top right**) of the observation respectively. The bottom panel, left to right, shows the evolution of the 10 minute-averaged closure phase with epoch (**bottom left**), *uv*-tracks for any particular night (**bottom middle**) and the visibility amplitudes $|V|$ of the unscattered (red) and scattered (grey-scale) sources as a function of *uv*-distance (**bottom right**). Variations of the flux on the shortest baselines reveal total flux modulation while flux variations $\Delta|V|$ on longer baselines and non-zero closure phases track the fluctuations in refractive noise. When compared to the latest published observations of Sgr A* [17], we see that the observed and simulated closure phase variability are consistent. Furthermore, ISM scattering simulations can constrain the variability fraction associated with the screen, enabling a more robust estimation of source variability.

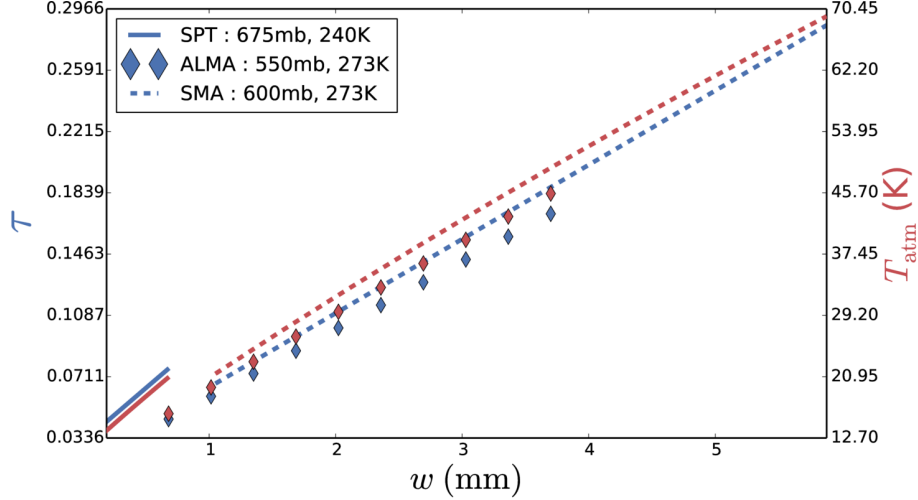


Figure 4.2: Best fit opacity (red) and sky brightness temperature (blue) line solutions at $\nu = 230$ GHz as a function of precipitable water vapour (PWV) for three indicative ground pressures and temperatures which approximately represent the sites of SPT (solid), ALMA (diamond) and SMA (dashed). The legend shows the estimated input ground (pressure, temperature) parameters for each site.

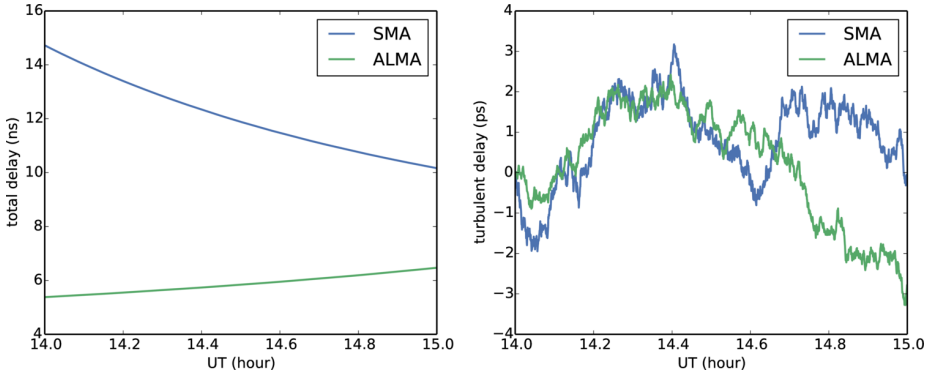


Figure 4.3: Simulation of the total delay (left) and the turbulent atmospheric delay (right) for SMA (blue) and ALMA (green) sites towards Sgr A*. Ground pressures and temperatures are the same as Fig. 4.2, precipitable water vapour above each station is set to $w = 2$ mm, and the instantaneous zenith coherence time is set $T_0 = 10$ s for both stations. Note that all tropospheric parameters are, however, independently set. The conversion from time delay to phase at 230 GHz is 1 rad = 0.7 ps.

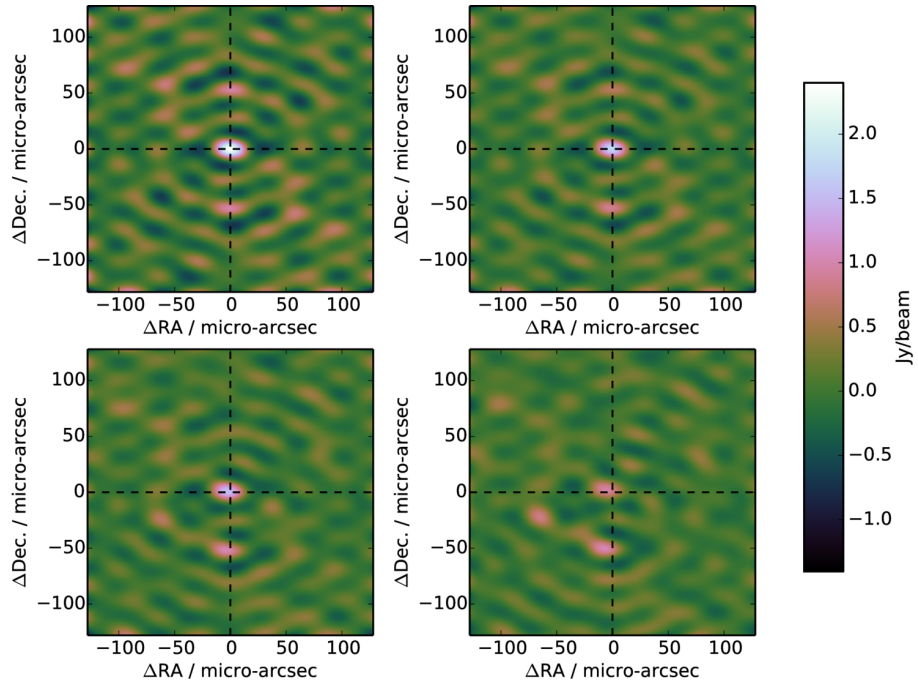


Figure 4.4: The effect of residual troposphere phase noise on interferometric images of a point source observed for 12 hours at 230 GHz with 4 GHz bandwidth with the following array : SPT, ALMA, SMA, SMT, LMT and JCMT, assuming the same SEFDs as (**author?**) [28] and an elevation limit of 15° . For simplicity the weather parameters at each station were set to: coherence time $t_0 = 10$ sec; PWV depth $w = 1$ mm; ground pressure $P = 600$ mb; ground temperature $T = 273$ K. **Top left:** interferometric map with thermal noise only. **Top right:** atmospheric attenuation and sky noise (due to non-zero opacity) with 1% of the turbulent phase noise added. **Bottom left:** as previous but with 3% of turbulent phase contribution. **Bottom right:** as previous but with 6% turbulent phase contribution. The fractional turbulent phase contributions are illustrative of the effect of fringe-fitting errors. Note the decrease in the source peak flux with increasing turbulent tropospheric phase noise. Note further that the peak source centroid is offset from its true position (black crosshairs).

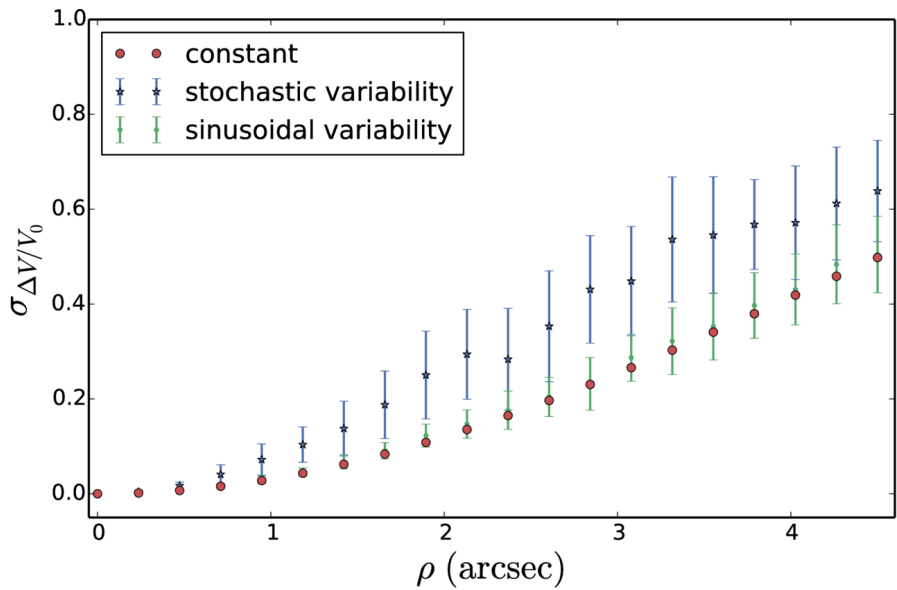


Figure 4.5: RMS relative amplitude error induced by pointing error with the 50 m (i.e. fully illuminated) LMT antenna as a function of pointing error offset ρ at 230 GHz. We assume that these errors are degenerate or non-separable from the self-calibration/fringe-fitting model used. See text for the description of the three models used. This simulation capability enables constraints on the magnitude of pointing-induced errors given a particular pointing calibration strategy.

In section ?? we explore the observational consequences of observing through a turbulent troposphere. In this simulation, we assume a simple point source model and apply increasing levels of turbulence-induced phase fluctuations before imaging using the two dimensional inverse fast Fourier transforms. We note a rapid attenuation in peak flux due to incoherent averaging, slight offsets in the source centroid and the presence of spurious imaging artefacts. Surprisingly, in this configuration, there was no evidence of blurring or a loss of resolution with the uncertainties. In an upcoming paper, we perform a systematic exploration of the turbulent tropospheric effects on the accuracy of fringe-fitting algorithms/strategies, through use of an automated calibration procedure and including the added complexity of a time-variable source.

Significant progress has been made in the theoretical and numerical modeling of the inner accretion flow and jet launch regions near a supermassive black hole event horizon. With MEQSILHOUETTE, we now have the ability to couple these with sophisticated interferometric and signal propagation simulations. This offers a tool to enable a more closely-knit and effective interplay between theoretical predictions and observational capabilities. Moreover, detailed interferometric simulations will enable us to quantify systematic effects on the black hole and/or accretion flow parameter estimation.

4.0.2 Parameter estimation

Chapter 5

Conclusion

In light of the science objectives of mm-VLBI observations and software advances in the broader radio interferometry community, a mm-VLBI data simulator has been developed. An important feature is that this simulation pipeline is performed using the MEASUREMENT SET format, in line with ALMA and future VLBI data formats. The focus has been placed on simulating realistic data given an arbitrary theoretical sky model. To this end, the simulator includes signal corruptions in the interstellar medium (ISM), troposphere and instrumentation. Examples of typical corruptions have been demonstrated, which show that each corruption can significantly affect the inferred scientific parameters. Particular focus has been placed on EHT observations, however, the pipeline is completely general with respect to observation configuration and source structure. Time variability in all domains (source, array, ISM, troposphere) is implemented. Future releases of MEQSILHOUETTE will include polarisation dependent corruptions. The creation of a close interface between sophisticated theoretical and interferometric mm-VLBI simulations will enhance the scientific opportunities possible with the EHT.

Bibliography

- [1] J. W. Armstrong, B. J. Rickett, and S. R. Spangler. Electron density power spectrum in the local interstellar medium. *ApJ*, 443:209, apr 1995.
- [2] Max Born and Emil Wolf. FOUNDATIONS OF GEOMETRICAL OPTICS. In *Principles of Optics*, pages 109–132. Elsevier BV, 1980.
- [3] K. L. Bouman, M. D. Johnson, D. Zoran, V. L. Fish, S. S. Doeleman, and W. T. Freeman. Computational Imaging for VLBI Image Reconstruction. *ArXiv e-prints*, dec 2015.
- [4] Geoffrey C. Bower, Adam Deller, Paul Demorest, Andreas Brunthaler, Ralph Eatough, Heino Falcke, Michael Kramer, K. J. Lee, and Laura Spitler. THE ANGULAR BROADENING OF THE GALACTIC CENTER PULSAR SGR J1745-29: A NEW CONSTRAINT ON THE SCATTERING MEDIUM. *ApJ*, 780(1):L2, dec 2013.
- [5] Geoffrey C. Bower, W. M. Goss, Heino Falcke, Donald C. Backer, and Yoram Lithwick. The Intrinsic Size of Sagittarius A* from 0.35 to 6 cm. *ApJ*, 648(2):L127–L130, aug 2006.
- [6] Avery E. Broderick, Vincent L. Fish, Michael D. Johnson, Katherine Rosenfeld, Carlos Wang, Sheperd S. Doeleman, Kazunori Akiyama, Tim Johannsen, and Alan L. Roy. MODELING SEVEN YEARS OF EVENT HORIZON TELESCOPE OBSERVATIONS WITH RADIATIVELY INEFFICIENT ACCRETION FLOW MODELS. *ApJ*, 820(2):137, mar 2016.
- [7] Avery E. Broderick, Tim Johannsen, Abraham Loeb, and Dimitrios Psaltis. TESTING THE NO-HAIR THEOREM WITH EVENT HORIZON TELESCOPE OBSERVATIONS OF SAGITTARIUS A*. *ApJ*, 784(1):7, feb 2014.
- [8] CL Brogan, LM Pérez, TR Hunter, WRF Dent, AS Hales, RE Hills, S Corder, EB Fomalont, C Vlahakis, Y Asaki, et al. The 2014 alma long baseline campaign: First results from high angular resolution observations toward the hl tau regionthis article is part of the alma long baseline campaign collection. an introduction and the full list of articles can be found at http://iopscience.iop.org/2041-8205/page/focus_on_the_alma_long_baseline_campaign. *The Astrophysical Journal Letters*, 808(1):L3, 2015.
- [9] C. L. Carilli and M. A. Holdaway. Tropospheric phase calibration in millimeter interferometry. *Radio Sci.*, 34(4):817–840, jul 1999.

- [10] CL Carilli and MA Holdaway. Application of Fast Switching Phase Calibration at mm Wavelengths on 33 km Baselines. *MMA/ALMA Memorandum Series No 173, National Radio Astronomy Organisation NRAO*, 1997.
- [11] C. E. Coulman. Fundamental and Applied Aspects of Astronomical “Seeing”. *Annual Review of Astronomy and Astrophysics*, 23(1):19–57, sep 1985.
- [12] Emily I Curtis, Bojan Nikolic, John S Richer, and Juan R Pardo. Atmospheric dispersion and the implications for phase calibration. *arXiv preprint arXiv:0912.2852*, 2009.
- [13] S. S. Doeleman, Z.-Q. Shen, A. E. E. Rogers, G. C. Bower, M. C. H. Wright, J. H. Zhao, D. C. Backer, J. W. Crowley, R. W. Freund, P. T. P. Ho, K. Y. Lo, and D. P. Woody. Structure of Sagittarius A* at 86 GH[CLC]z/[CLC] using VLBI Closure Quantities. *The Astronomical Journal*, 121(5):2610–2617, may 2001.
- [14] Sheperd S. Doeleman, Vincent L. Fish, Avery E. Broderick, Abraham Loeb, and Alan E. E. Rogers. DETECTING FLARING STRUCTURES IN SAGITTARIUS A* WITH HIGH-FREQUENCY VLBI. *ApJ*, 695(1):59–74, mar 2009.
- [15] Sheperd S. Doeleman, Jonathan Weintraub, Alan E. E. Rogers, Richard Plambeck, Robert Freund, Remo P. J. Tilanus, Per Friberg, Lucy M. Ziurys, James M. Moran, Brian Corey, Ken H. Young, Daniel L. Smythe, Michael Titus, Daniel P. Marrone, Roger J. Cappallo, Douglas C.-J. Bock, Geoffrey C. Bower, Richard Chamberlin, Gary R. Davis, Thomas P. Krichbaum, James Lamb, Holly Maness, Arthur E. Niell, Alan Roy, Peter Strittmatter, Daniel Werthimer, Alan R. Whitney, and David Woody. Event-horizon-scale structure in the supermassive black hole candidate at the Galactic Centre. *Nature*, 455(7209):78–80, sep 2008.
- [16] Vincent L. Fish, Sheperd S. Doeleman, Christopher Beaudoin, Ray Blundell, David E. Bolin, Geoffrey C. Bower, Richard Chamberlin, Robert Freund, Per Friberg, Mark A. Gurwell, Mareki Honma, Makoto Inoue, Thomas P. Krichbaum, James Lamb, Daniel P. Marrone, James M. Moran, Tomoaki Oyama, Richard Plambeck, Rurik Primiani, Alan E. E. Rogers, Daniel L. Smythe, Jason SooHoo, Peter Strittmatter, Remo P. J. Tilanus, Michael Titus, Jonathan Weintraub, Melvyn Wright, David Woody, Ken H. Young, and Lucy M. Ziurys. 1.3 mm WAVELENGTH VLBI OF SAGITTARIUS A*: DETECTION OF TIME-VARIABLE EMISSION ON EVENT HORIZON SCALES. *ApJ*, 727(2):L36, jan 2011.
- [17] Vincent L. Fish, Michael D. Johnson, Sheperd S. Doeleman, Avery E. Broderick, Dimitrios Psaltis, Ru-Sen Lu, Kazunori Akiyama, Walter Alef, Juan Carlos Algaba, Keiichi Asada, Christopher Beaudoin, Alessandra Bertarini, Lindy Blackburn, Ray Blundell, Geoffrey C. Bower, Christiaan Brinkerink, Roger Cappallo, Andrew A. Chael, Richard Chamberlin, Chi-Kwan Chan, Geoffrey B. Crew, Jason Dexter, Matt Dexter, Sergio A. Dzib, Heino Falcke, Robert Freund, Per Friberg, Christopher H. Greer, Mark A. Gurwell, Paul T. P. Ho, Mareki Honma, Makoto Inoue, Tim Johannsen,

- Junhan Kim, Thomas P. Krichbaum, James Lamb, Jonathan León-Tavares, Abraham Loeb, Laurent Loinard, David MacMahon, Daniel P. Marrone, James M. Moran, Monika Mościbrodzka, Gisela N. Ortiz-León, Tomoaki Oyama, Feryal Özel, Richard L. Plambeck, Nicolas Pradel, Rurik A. Primiani, Alan E. E. Rogers, Katherine Rosenfeld, Helge Rottmann, Alan L. Roy, Chester Ruszczyk, Daniel L. Smythe, Jason SooHoo, Justin Spilker, Jordan Stone, Peter Strittmatter, Remo P. J. Tilanus, Michael Titus, Laura Vertatschitsch, Jan Wagner, John F. C. Wardle, Jonathan Weintroub, David Woody, Melvyn Wright, Paul Yamaguchi, André Young, Ken H. Young, J. Anton Zensus, and Lucy M. Ziurys. PERSISTENT ASYMMETRIC STRUCTURE OF SAGITTARIUS A* ON EVENT HORIZON SCALES. *ApJ*, 820(2):90, mar 2016.
- [18] Vincent L. Fish, Michael D. Johnson, Ru-Sen Lu, Sheperd S. Doeelman, Katherine L. Bouman, Daniel Zoran, William T. Freeman, Dimitrios Psaltis, Ramesh Narayan, Victor Pankratius, Avery E. Broderick, Carl R. Gwinn, and Laura E. Vertatschitsch. IMAGING AN EVENT HORIZON: MITIGATION OF SCATTERING TOWARD SAGITTARIUS A*. *ApJ*, 795(2):134, oct 2014.
- [19] J. Goodman and R. Narayan. The shape of a scatter-broadened image - II. Interferometric visibilities. *Monthly Notices of the Royal Astronomical Society*, 238(3):995–1028, jun 1989.
- [20] C. R. Gwinn, Y. Y. Kovalev, M. D. Johnson, and V. A. Soglasnov. DISCOVERY OF SUBSTRUCTURE IN THE SCATTER-BROADENED IMAGE OF SGR A*. *ApJ*, 794(1):L14, sep 2014.
- [21] J. P. Hamaker, J. D. Bregman, and R. J. Sault. Understanding radio polarimetry. I. Mathematical foundations. *Astronomy and Astrophysics Supplement Series*, 117(1):137–147, may 1996.
- [22] DC Hogg, FO Guiraud, and MT Decker. Measurement of excess radio transmission length on earth-space paths. *Astronomy and Astrophysics*, 95:304–307, 1981.
- [23] M. D. Johnson, V. L. Fish, S. S. Doeelman, D. P. Marrone, R. L. Plambeck, J. F. C. Wardle, K. Akiyama, K. Asada, C. Beaudoin, L. Blackburn, R. Blundell, G. C. Bower, C. Brinkerink, A. E. Broderick, R. Cappallo, A. A. Chael, G. B. Crew, J. Dexter, M. Dexter, R. Freund, P. Friberg, R. Gold, M. A. Gurwell, P. T. P. Ho, M. Honma, M. Inoue, M. Kosowsky, T. P. Krichbaum, J. Lamb, A. Loeb, R.-S. Lu, D. MacMahon, J. C. McKinney, J. M. Moran, R. Narayan, R. A. Primiani, D. Psaltis, A. E. E. Rogers, K. Rosenfeld, J. SooHoo, R. P. J. Tilanus, M. Titus, L. Vertatschitsch, J. Weintroub, M. Wright, K. H. Young, J. A. Zensus, and L. M. Ziurys. Resolved magnetic-field structure and variability near the event horizon of Sagittarius A. *Science*, 350(6265):1242–1245, dec 2015.
- [24] Michael D. Johnson and Carl R. Gwinn. THEORY AND SIMULATIONS OF REFRACTIVE SUBSTRUCTURE IN RESOLVED SCATTER-BROADENED IMAGES. *ApJ*, 805(2):180, jun 2015.

- [25] A. P. Lane. Submillimeter Transmission at South Pole. In G. Novak and R. Landsberg, editors, *Astrophysics From Antarctica*, volume 141 of *Astronomical Society of the Pacific Conference Series*, pages 289–295, 1998.
- [26] R G Lane, A Glindemann, and J C Dainty. Simulation of a Kolmogorov phase screen. *Waves in Random Media*, 2(3):209–224, jul 1992.
- [27] O. P. Lay. The temporal power spectrum of atmospheric fluctuations due to water vapor. *Astronomy and Astrophysics Supplement Series*, 122(3):535–545, may 1997.
- [28] Ru-Sen Lu, Avery E. Broderick, Fabien Baron, John D. Monnier, Vincent L. Fish, Sheperd S. Doeleman, and Victor Pankratius. IMAGING THE SUPERMASSIVE BLACK HOLE SHADOW AND JET BASE OF M87 WITH THE EVENT HORIZON TELESCOPE. *ApJ*, 788(2):120, may 2014.
- [29] COLIN R Masson. Atmospheric effects and calibrations. In *IAU Colloq. 140: Astronomy with Millimeter and Submillimeter Wave Interferometry*, volume 59, pages 87–95, 1994.
- [30] John D. Monnier. Phases in interferometry. *New Astronomy Reviews*, 51(8-9):604–616, oct 2007.
- [31] R. Narayan. The Physics of Pulsar Scintillation. *Philosophical Transactions of the Royal Society A: Mathematical Physical and Engineering Sciences*, 341(1660):151–165, oct 1992.
- [32] R. Narayan and J. Goodman. The shape of a scatter-broadened image - I. Numerical simulations and physical principles. *Monthly Notices of the Royal Astronomical Society*, 238(3):963–994, jun 1989.
- [33] Bojan Nikolic, Rosie C Bolton, Sarah F Graves, Richard E Hills, and John S Richer. Phase correction for ALMA with 183 GHz water vapour radiometers. *Astronomy & Astrophysics*, 552:A104, 2013.
- [34] J. E. Noordam and O. M. Smirnov. The MeqTrees software system and its use for third-generation calibration of radio interferometers. *Astronomy & Astrophysics*, 524:A61, nov 2010.
- [35] G. N. Ortiz-León, M. D. Johnson, S. S. Doeleman, L. Blackburn, V. L. Fish, L. Loinard, M. J. Reid, E. Castillo, A. A. Chael, A. Hernández-Gómez, D. Hughes, J. León-Tavares, R.-S. Lu, A. Montaña, G. Narayanan, K. Rosenfeld, D. Sánchez, F. P. Schloerb, Z.-q. Shen, H. Shiokawa, J. SooHoo, and L. Vertatschitsch. The Intrinsic Shape of Sagittarius A* at 3.5-mm Wavelength. *ArXiv e-prints*, jan 2016.
- [36] J.R. Pardo, J. Cernicharo, and E. Serabyn. Atmospheric transmission at microwaves (ATM): an improved model for millimeter/submillimeter applications. *IEEE Trans. Antennas Propagat.*, 49(12):1683–1694, 2001.
- [37] A. Popping and R. Braun. The standing wave phenomenon in radio telescopes. *Astronomy and Astrophysics*, 479(3):903–913, mar 2008.

- [38] Dimitrios Psaltis, Norbert Wex, and Michael Kramer. A QUANTITATIVE TEST OF THE NO-HAIR THEOREM WITH Sgr A* USING STARS PULSARS AND THE EVENT HORIZON TELESCOPE. *ApJ*, 818(2):121, feb 2016.
- [39] S. J. Radford and M. A. Holdaway. Atmospheric conditions at a site for submillimeter-wavelength astronomy. In T. G. Phillips, editor, *Advanced Technology MMW, Radio, and Terahertz Telescopes*, volume 3357 of , pages 486–494, jul 1998.
- [40] Alan E. E. Rogers, Sheperd S. Doeleman, and James M. Moran. Fringe detection methods for very long baseline arrays. *The Astronomical Journal*, 109:1391, mar 1995.
- [41] E. Serabyn, E. W. Weisstein, D. C. Lis, and J. R. Pardo. Submillimeter Fourier-transform spectrometer measurements of atmospheric opacity above Mauna Kea. *Appl. Opt.*, 37(12):2185, apr 1998.
- [42] O. M. Smirnov. Revisiting the radio interferometer measurement equation. *AA*, 527:A106, 2011.
- [43] O. M. Smirnov. Revisiting the radio interferometer measurement equation. *AA*, 527:A107, 2011.
- [44] O. M. Smirnov. Revisiting the radio interferometer measurement equation. *AA*, 527:A108, 2011.
- [45] A. R. Thompson, J. M. Moran, and G. W. Swenson, Jr. *Interferometry and Synthesis in Radio Astronomy, 2nd Edition*. 2001.
- [46] R. N. Treuhaft and G. E. Lanyi. The effect of the dynamic wet troposphere on radio interferometric measurements. *Radio Sci.*, 22(2):251–265, mar 1987.